Nat Hazards (2018) 90:1277–1307
https://doi.org/10.1007/s11069-017-3119-5

ORIGINAL PAPER

The intriguing tsunami of 19 March 2017 at Bandar Dayyer, Iran: field survey and simulations

Amir Salaree[1] · **Reza Mansouri**[2] · **Emile A. Okal**[1]

Received: 2 August 2017 / Accepted: 30 October 2017 / Published online: 17 November 2017

Abstract We present a field survey and a number of simulations of the local Persian Gulf tsunami of 19 March 2017 at Bandar Dayyer, Iran, which resulted in one death, five persons missing and significant damage to the port. The field survey defined the inundated area as extending $\sim$ 40 km along the coast, with major effects concentrated on an $\sim$ 8 km stretch immediately west of Dayyer, a maximum run-up of 3 m and maximum inundation reaching 600 m. In the absence of significant earthquakes on that day, we first test the possibility of generation of a landslide; however, our simulations for legitimate sources fail to reproduce the distribution of run-up along the coast. We prefer the model of a meteorological tsunami, triggered by Proudman resonance with a hypothetical weather front moving at 10 m/s in a NNW azimuth, which could be an ancillary phenomenon to a major shamal wind system present over the Persian Gulf on that day. More detailed simulations of the Dayyer tsunami would require an improved bathymetric grid in the vicinity of the relevant coastal segment.

Keywords Tsunami · Meteotsunami · Persian Gulf · Field survey · Simulation

✉ Amir Salaree
amir@earth.northwestern.edu

Reza Mansouri
s.r.mansouri@pgu.ac.ir

Emile A. Okal
emile@earth.northwestern.edu

[1] Department of Earth and Planetary Sciences, Northwestern University, Evanston, IL 60208, USA

[2] Persian Gulf University, Shahid Mahini Blvd, Bandar Bushehr, Bushehr, Iran

1 Introduction

On 19 March 2017, a series of waves from the Persian Gulf inundated significant parts of the Port of Dayyer on the southern coastlines of Iran (Fig. 1), some time between 8:00 and 8:20 AM local time (4:30−4:50 GMT). It resulted in one death and five people missing, and reportedly capsized about 300 boats and caused $\sim$ \$10 million of damage. According to Iranian state media, water progressed as far as $\sim$ 1 km in land and video footage recorded by local individuals or seasonal travelers reveals surges of up to $\sim$ 2 m in a relatively calm, cloudy morning, even though a significant thunderstorm had occurred a few hours earlier. Local news outlets place the largest extent of destruction at Seyyed-Safa, a neighborhood close to the cruise port (Fig. 2).

Such accounts of the event lack the quantitative nature necessary for a scientific understanding of the phenomenon. First, the initial reports of the tsunami do not reveal the full extent of inundation as they only provide descriptive—albeit very valuable—accounts of the surge at Dayyer. In particular, it is not clear whether the surge was indeed focused on Dayyer, or was simply reported there due to the presence of people and infrastructure. Second, although the maximum run-up was reported to reach 2 m, it is also unclear if it had been the highest value through the entire extent of inundation. Such information is critical in determining the type of tsunami source as well as its energy (e.g., Okal et al. 2002; Okal

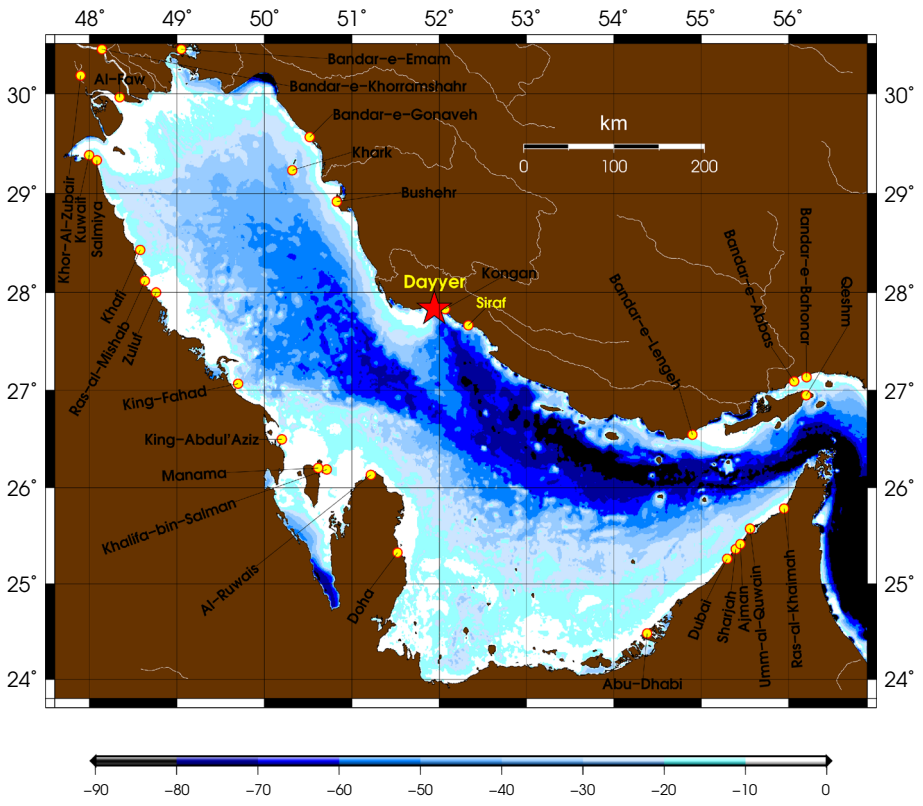

Fig. 1 Bathymetry (GEBCO; Fisher et al. 1982) of the Persian Gulf and major population centers at the coastlines. Major rivers are shown with white lines. The red star represents the port of Dayyer

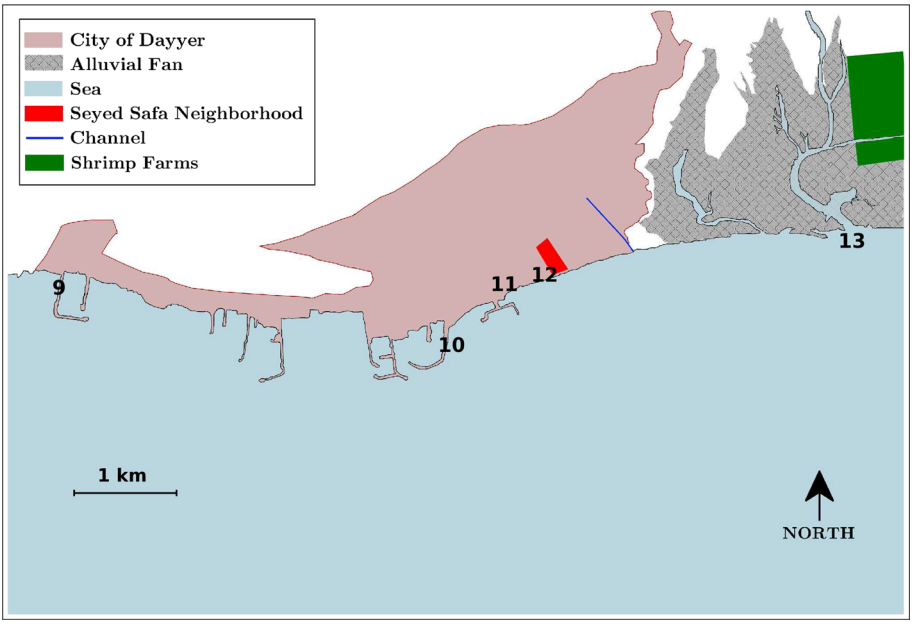

Fig. 2 Map view of the port of Dayyer. The Seyyed-Safa neighborhood is depicted by a filled red rectangle. Numbers correspond to the survey points as listed in Table 1

and Synolakis 2004; Ten Brink et al. 2009). Third, the number of the incoming waves was not clear from the few remarks about a multitude of waves in the available video footage from the event. This is potentially a valuable piece of data especially when dealing with phenomena such as dispersion, source polarity and basin effects (e.g., Rabinovich 1997; Okal et al. 2009; Fritz et al. 2012). Finally, although a significant storm (see Sect. 3.3.1.1) preceded the surge, there were indications of calm weather during the event in some of the footage. This could play a critical role in reconstructing the event by studying it as a meteorological phenomenon. In this general context, it was decided to perform a systematic survey of the effects of the 2017 event in and around Dayyer to obtain a quantitative database allowing hydrodynamic modeling.

Any study of this type of wave must be carried out in the more general framework of the history of tsunamis in the Persian Gulf. The latter consists of only a few events mentioned in either archeological or seismological records of the region (e.g., Whitehouse 1968; Ambraseys 1982), and remains vague and probably incomplete due to the lack of systematic paleoseismic and paleotsunami studies in the area. Information on historical tsunamis is usually found in existing earthquake catalogs (Ambraseys 2008) which although useful, often provide few details about the precise nature of the waves, and can also involve a degree of speculation.

Perhaps the only detailed account of a tsunami in the Persian Gulf is given for the 1008 A.D. Siraf event. According to historical accounts (e.g., Ambraseys 1982), an earthquake ($M \approx 6.5$) with about 10,000 casualties created a surge at the ancient port of Siraf (near today's city of Siraf, about 45 km southeast of Dayyer; see Fig. 1) which sank a number of ships and damaged the city's main port. There is an ongoing debate about the occurrence of this tsunami as well as the destruction of Siraf by this event. For instance, based on submarine archeological findings, Tofighian (2014) attributes the decline of the then major

Table 1 Results from the field survey on 17 May 2017

No.	Location	Lon.	Lat.	Run-up (m)	Inund. (m)	Evidence
1	Motaf Park (I)	51.58194	27.84417	$\gtrapprox 0.3$	N/A	Water overtopped (due north) a $\sim$ 1.3 m ridge; sand and salt deposits on the northern side of the ridge
2	Motaf Park (II)	51.59367	27.84400	N/A	N/A	Deposited salt on land
3	Motaf Park (III)	51.60296	27.84821	$\gtrapprox 1.3$	N/A	Water has overtopped the ridge
4	Motaf Park (IV)	51.60628	27.85233	N/A	N/A	Water inundating a plain by the sea
5	Kali	51.65871	27.84307	1.5 (1.42)	40–50 (41)	Utility pole collapsed; boats rocks moved inland; flooding has exposed tree roots; only one wave was observed
6	Demigez (I)	51.68288	27.83206	1.8	110–120 (119)	Western side of the jetty damaged; distinct salt deposits across the plain; boats moved and damaged
7	Demigez (II)	51.72643	27.83347	N/A	N/A	Timbers and rocks moved on a large scale
8	Bibi-Khatoon	51.80413	27.84660	> 2.0	600	Salt deposits across the plain; utility poles along the coast were soaked, leaving distinct marks; fishing nets and tools were displaced and damaged; pieces of timber and rocks moved due north inland
9	North Oli	51.90383	27.83300	~ 3.0	230 (along channel)	Water overtopped the rocky jetty
10	Dayyer (fishing jetty)	51.93079	27.83073	2.5	60	Water inundated the city; Eastern side of the fishing jetty was damaged; three dhows docked at the jetty sank; three waves (one large and two smaller) were observed
11	Dayyer (municipal jetty)	51.93736	27.83329	2.5	170	Jetty demolished; boats damaged from striking the seawalls while being washed into the city
12	Dayyer (coast)	51.94269	27.83504	2.5	190	The seawall partly destroyed; Coastal shops demolished/displaced; windows of shops further inland were broken; rocks deposited on land
13	Bardestan Estuary	51.98526	27.84687	> 1.0	140	Water reached the shrimp farms along the channels, but did not pour into pools.
14	Banak Park	52.01888	27.84243	0.1–0.9 (?)	10	Water did not transgress the park due to its relative higher altitude (by $\sim$ 3 m)
15	Kangan	52.05185	27.83608	0	0	No significant surge

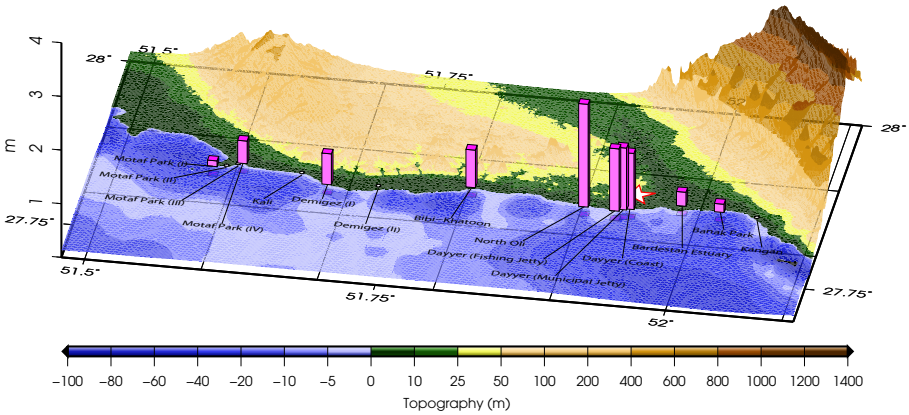

Fig. 3 The interview points from the survey are marked with vertical columns where the height of the column corresponds to the measured run-ups. The white star represents Dayyer

port of Siraf to erosion of the port's infrastructure. Several other studies (e.g., Lamb 1964; Whitehouse 1968) attribute the city's decline to an earlier earthquake in 978 A.D. ($M \approx 5.3$; Ambraseys 1982), which resulted in aftershocks lasting for seven days and destroyed the harbor (e.g., Whitehouse 1968).

2 Field survey

The survey along the Iranian coastline of the Persian Gulf in the vicinity of Dayyer was conducted on 17 May 2017 to gather quantitative data regarding the 19 March 2017 tsunami. The survey started from Motaf Park in the west and was concluded in Banak Park in the east (Fig. 3), over a total of $\sim$ 50 km of coastline. Some portions of the coastline could not be covered in the survey due to logistical issues.

The data were collected through routine methods of post-tsunami surveys (e.g., Abe et al. 1993; Synolakis et al. 1995; Okal et al. 2002) by interviewing more than 30 eye-witnesses and making measurements of the evidence left from the surge. Results are listed in Table 1 and Fig. 3.

We recall that *run-up* is defined as the elevation above sea level of the point of maximum penetration of the wave, *flow depth* as the height of the water flowing over an initially dry point of reference (usually the coastline), and *inundation* as the horizontal distance of maximum penetration from the coastline.

Measuring run-up and/or inundation at some of the points in Table 1 was not possible due to the lack of definitive geological evidence or credible accounts from the locals; we have then listed other useful evidence at these locations.

2.1 Field evidence

Because at the time of the survey, 2 months had already passed since the tsunami, some of the physical evidence from it was displaced or eroded. The amount of the remaining evidence and the effects of the surge according to the testimonies of eyewitnesses increased as the team moved east toward Dayyer. While such evidence was limited to

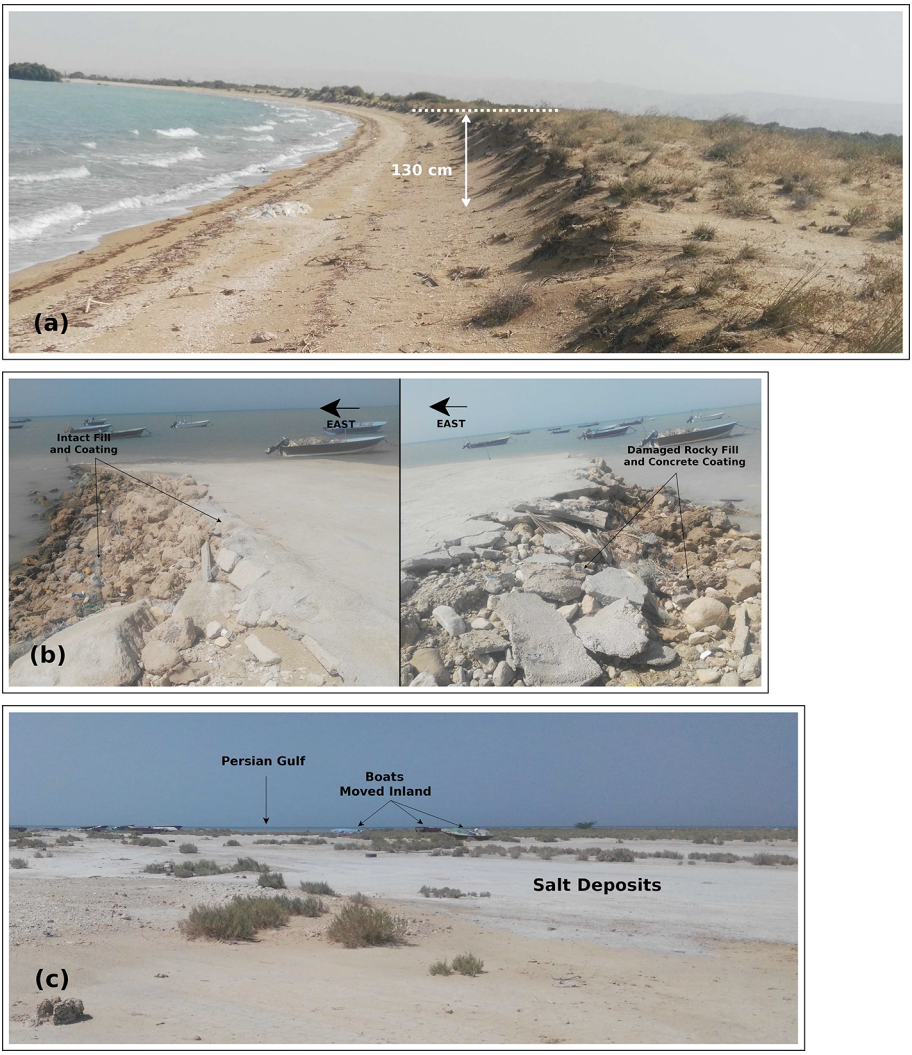

Fig. 4 Evidence from points 1–7 of the survey. **a** The ridge at Motaf which was allegedly overtopped by the surge. **b** The fishing jetty at Kali with its western side damaged as a result of the surge. **c** Salt deposits and wrecked boats from the surge

possible sand deposits in the west, the size of the debris moved by the event increased significantly as we moved to the east.

The tsunami occurred between 8:00 and 8:20 AM (local time) on 19 March 2017, which was close to high tide at Dayyer (6:00 AM; Rodis 2017). Therefore, all the measurements in the survey were done relative to the sea level at high tide.

- At the Motaf Park (points 1–4 in Table 1), deposits were limited to sand and salt. Although the salt deposits might have been accumulated over time, this seems unlikely due to the presence of a 1.3 m ridge along the coastline (Fig. 4a); any event causing these deposits must have created waves large enough to overtop the ridge, and

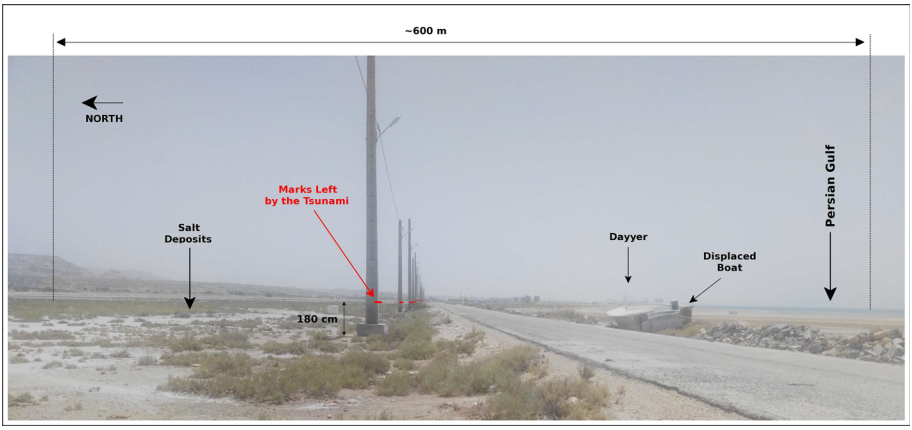

Fig. 5 Evidence for run-up and inundation at Bibi-Khatoon (point 8). Red marks on the utility poles depict flood level. Port of Dayyer can be seen in the background to the East

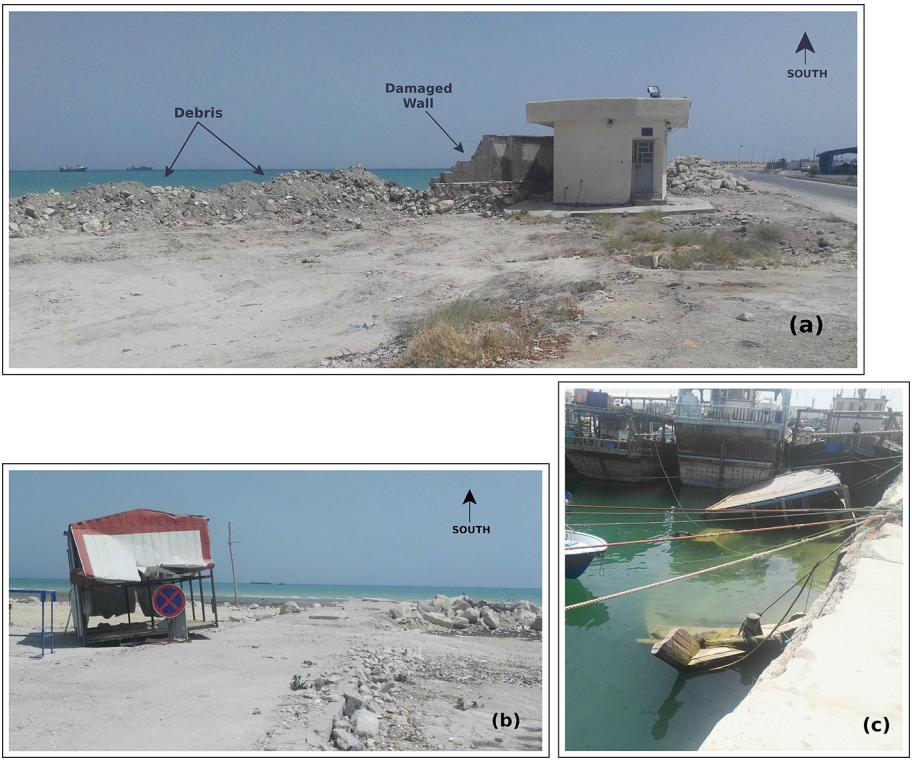

Fig. 6 Tsunami destruction at the city of Dayyer. **a** The northeast–southwest wall was damaged by the March 19 event. Debris from the wall along with rocks and sand from the surge as accumulated by the sea. **b** Coastal shop destroyed and moved by the surge. **c** Dhow sunk at the fishing jetty in Dayyer

obviously such an event would not have happened unnoticed. We found a variety of debris (plastic bottles, small pieces of wood, etc.) inland, but we could not resolve if they were indeed left by the surge in question.

- At Kali, a small village $\sim$ 30 km west of Dayyer (point 5), and according to the testimony of eyewitnesses, the surge had uprooted utility poles (put back in place after the event) and exposed roots of small trees. While much of the damage caused by the event had been repaired over the intervening 2 months, damaged building bricks and sand deposits were still visible in the village.
- At Demigez (points 6 and 7 in Table 1), a fishing area 23 km west of Dayyer, the survey found evidence of damage to the western side of the jetty (Fig. 4b). This is suggestive of a surge either from the west or with a strong westerly component as the destructive force. There were also damaged boats and broken timber along with salt, deposited at the time of inundation on land in Demigez (points 6–7; Fig. 4c).
- Bibi-Khatoon was perhaps the location where we encountered the most classic evidence of run-up and inundation. Utility poles along the east–west coastal road at a distance of $\sim$ 400 m from the sea had, almost uniformly, distinct marks from the flooding. There were debris by the roadside along with a boat displaced from the sea. The survey also found widespread salt deposits from the surge across the plain (Fig. 5).
- The highest run-up (3 m) was documented at North Oli (point 9 in Table 1), a fishing village $\sim$ 4 km to the west of Dayyer. According to the locals, the waves from the surge overtopped the harbor (**9** in Fig. 2) and progressed in land up to 230 m along a channel by the village, but did not transgress the village.
- The city of Dayyer (points 10–12 in Table 1) was most affected by the tsunami. Waves, up to 2.5 m high, capsized the boats and moved them into the city while damaging the coastal walls (Fig. 6a). A long wall with a predominantly north-side trend was partly damaged closer to the sea, while many east–west, albeit smaller, walls were still standing. During the surge, water inundated the city up to 190 m, and demolished or moved the coastal shops by several meters (Fig. 6b), shattering the windows of more inland, south-facing stores. Piles of boulders, rocks and smaller debris from the event were still noticeable by the time of the survey. According to eyewitnesses, three waves attacked the port sinking three dhows that had docked at the fishing jetty at the time of the event (Fig. 6c). These waves were described as a large wave followed by two smaller ones.

  Up to this point (city of Dayyer), local fishermen unanimously recalled calm, cloudy weather with a gentle breeze at the time of the event. From Bibi-Khatoon to Dayyer, however, we documented accounts of slightly stronger landward winds. Among the witnesses interviewed during the survey, none gave any accounts of either rain or strong wind at the time of the event.
- At $\sim$ 3 km east of Dayyer, the Bardestan estuary (point 13 in Table 1) was inundated by the tsunami. Water had reached the shrimp farms (see Fig. 2) $\sim$ 500 m from the sea along a channel, but had not made it into the pools which are $>$ 1 m above the high tide level, and thus, the waves were at most 1 m high at this location. Witnesses told the survey of heavy rain and strong wind at the time of the tsunami at Bardestan. However, we did not find any conclusive accounts about the timing of the surges and witnesses may have mistaken storm disturbances with the main surge.
- Although Banak Park (point 14, $\sim$ 8 km east of Dayyer) had experienced some waves, they were small and we were not able to obtain any consistent testimony from the local witnesses about their heights. Based on their accounts, waves ranged between 10 cm, barely touching the coastal benches, and 90 cm, large enough to move a few rocks and

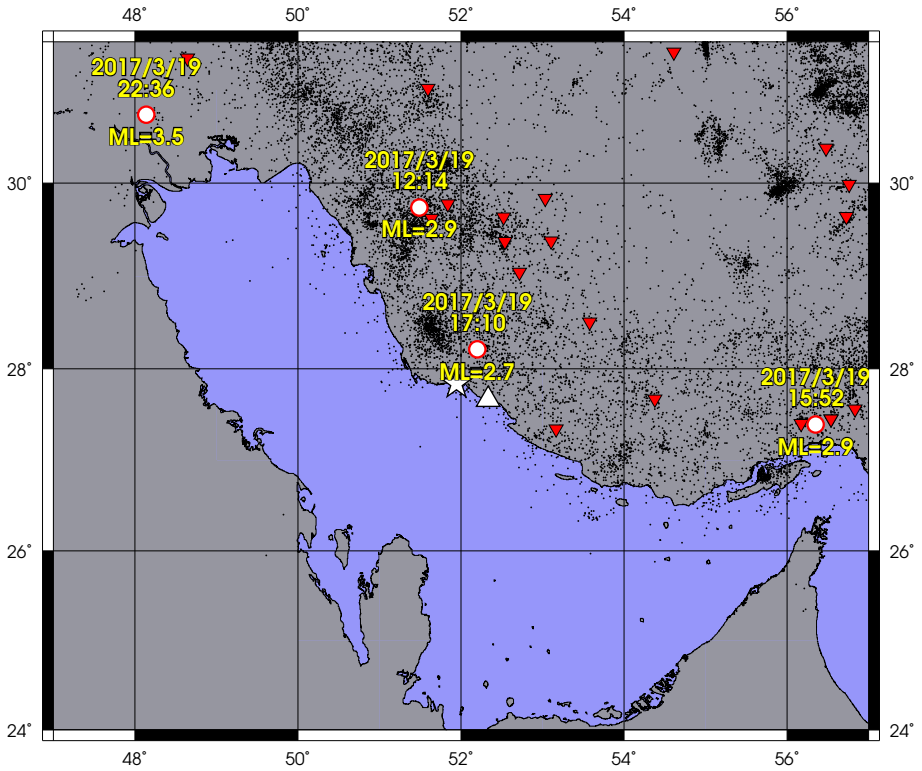

Fig. 7 Earthquakes recorded by IRSC on 19 March 2017 are shown with white circles. The background black dots represent the IRSC events during 2006–2016. Dayyer and Siraf are shown with white star and triangle, respectively. Red inverted triangles are IRSC stations

leave them on the shore. In the absence of definitive geological evidence to measure run-up, it is very difficult to estimate wave heights, especially due to the rainy weather—along with a gentle breeze—at this location.

- Finally, the tsunami was not noticed at Kangan Port, $\sim$ 12 km east of Dayyer. There was an unconfirmed report from Nakhl-Taghi, a city $\sim$ 80 km to the south, near Assalooyeh, of a boat having moved $\sim$ 100 m in land by a rogue wave; however, we found no confirmation of such an incident as no other witnesses knew about it.

2.2 Former events?

We interviewed Mr. Bagher Sohooli, age 85, who recalled the occurrence of a similar event in Dayyer $\sim$ 40–50 years ago, which he had personally experienced. We documented similar, albeit second hand, accounts of such an event in Kangan (point 15 in Table 1). However, Ali Sohooli, a fisherman, in North Oli had never experienced such a surge before.

We were not able to find more details about events in the past, and no other witnesses farther away from Dayyer had experienced or heard of such an incident which suggests that any potential former similar surges may only have affected Dayyer.

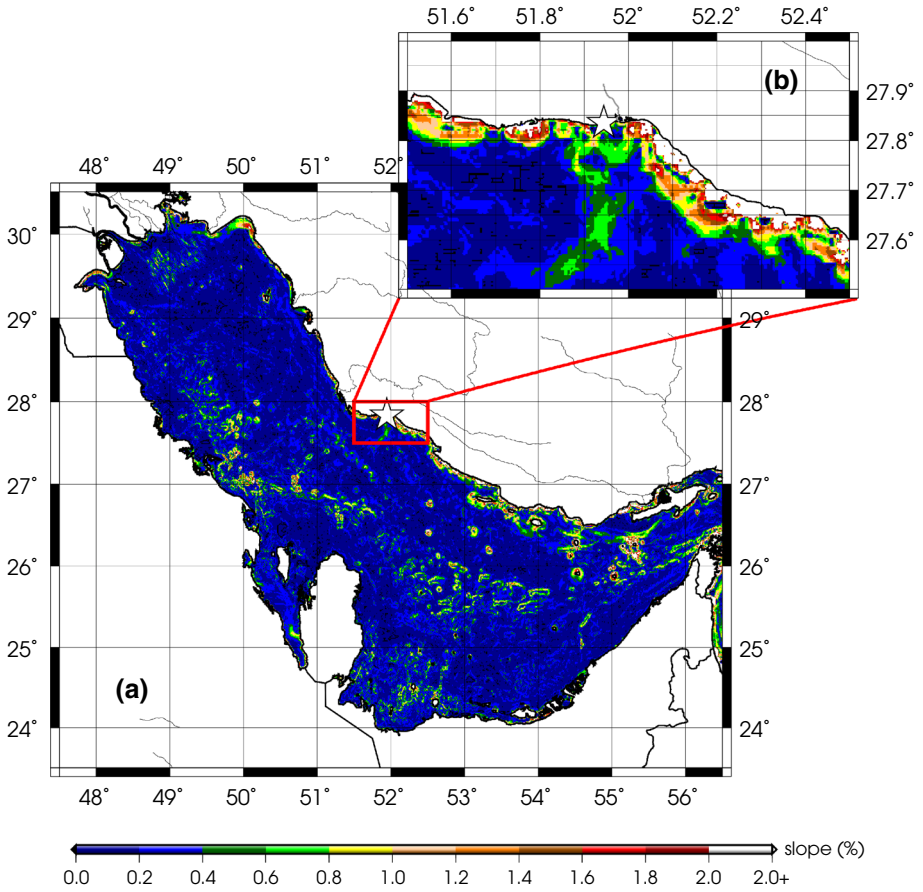

Fig. 8 **a** Slope map of the Persian Gulf calculated as the gradient of the GEBCO (Fisher et al. 1982) bathymetry with gray lines as permanent rivers. **b** Marine slope regime of the Dayyer area. The white stars in both figures depict Dayyer

2.3 Survey summary

As we can see in Table 1, noticeable inundations from the tsunami took place on a $\sim$ 40 km stretch of coastline with highest values of run-up focused on a $\sim$ 5 km band at and around the city of Dayyer, and the highest value of 3 m documented at the village of Oli, to the west of Dayyer. This is, more or less, in agreement with the initial reports of the surge from news outlets. However, the highest documented run-up (Oli) occurred at a $\sim$ 4 km distance from the main group of survey locations and constitutes an apparent outlier in the general trend of run-up values (i.e. gradually increasing from west and approaching Dayyer); it might be explained as a seiching effect created by the harbor structure (e.g., Borrero et al. 2015; Synolakis et al. 2016) at Oli (**9** in Fig. 2).

We found extensive deposits from the tsunami extending from Motaf Park to Dayyer. The deposits range from salt and sand in the west to $\sim$ 1 m boulders in the east, with the majority of the destruction at Dayyer in the form of demolished kiosks and shops, wrecked dhows, damaged or capsized boats, and collapsed walls. The intensity of damages

decreased moving further to the east from Dayyer, as no surge was observed in the Kangan Port, $\sim$ 8 km away.

3 Modeling efforts

3.1 Earthquake?

In this section, we first rule out the possibility of an earthquake source for the Dayyer tsunami. In view of the generally high seismicity rate of southern Iran, it would be legitimate to raise the question of a seismic source for the 19 March 2017 tsunami. However, no moderate to large earthquakes capable of generating a tsunami with such run-ups as those documented during the survey were recorded by any seismological agencies on the day in question. As shown on Fig. 7, the largest earthquakes recorded by the Iranian Seismological Center (IRSC) occurred on land and none were large enough to create a

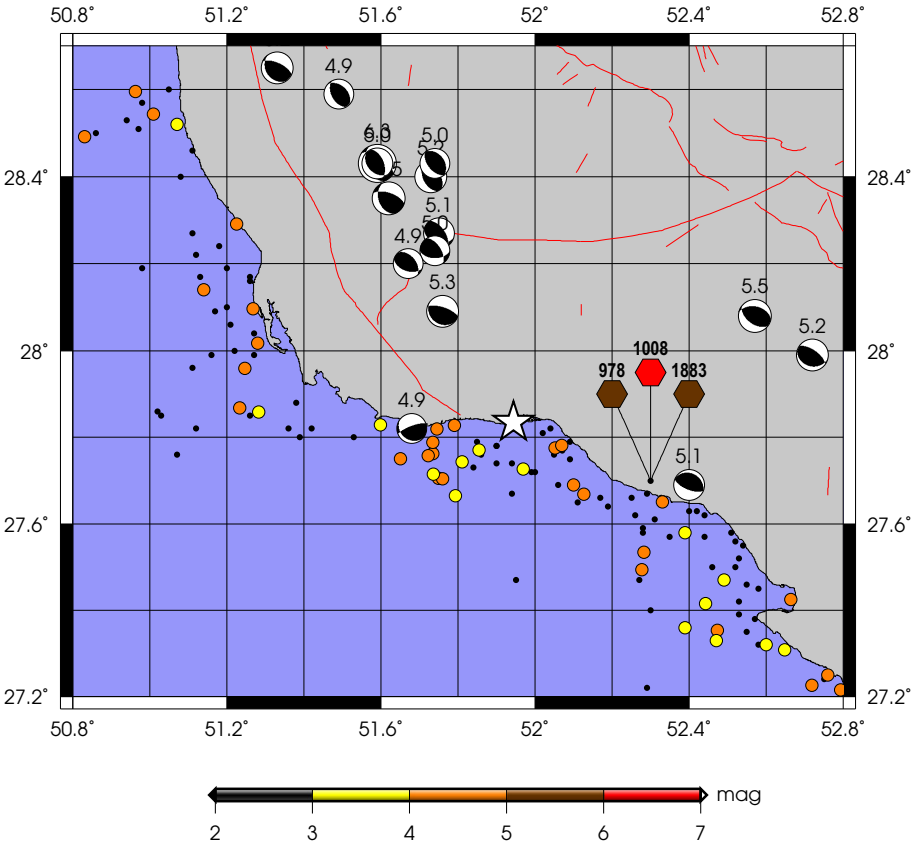

Fig. 9 Seismicity of Dayyer region. While the marine events from the USGS catalog are shown with color coded circles (according to their magnitudes), the black dots represent the smaller events from the local IRSC catalog (e.g., Mirzaei et al. 2002). The beach balls are focal solutions from the Harvard CMT catalog (Dziewonski et al. 1981; Ekström et al. 2012). Hexagons are the historical events from Ambraseys and Melville (1982). Red lines show the known on-land faults. Dayyer is shown with a white star

tsunami. According to seismic scaling laws (e.g., Geller 1976), these earthquakes of magnitudes $M_L < 3$ would feature fault dislocations of $\sim$ 1 cm, resulting in possible run-ups of the same order (e.g., Plafker 1997; Okal and Synolakis 2004) for a generally linear coastline and in the absence of bays (e.g., Abe 2005), about a hundred times less than observed. Additionally, their origin times grossly mismatch the arrival time of the tsunami.

3.2 Landslide

The local nature of the tsunami along with the relatively calm weather during which it took place suggest that the surge may have been caused by of a submarine landslide. Such phenomena have been extensively documented and studied (e.g., Synolakis et al. 2002; Okal and Synolakis 2003; Ma et al. 2013; Weiss et al. 2013; Miller et al. 2017).

Submarine landslides follow the direction of steepest descent of the bathymetry (e.g., Okal and Synolakis 2004; Salaree and Okal 2015) and tend to occur at slopes between $\sim$ 3 and $\sim$ 6%, but can also take place on slopes as low as $\sim$ 1% in very shallow waters (e.g., Skempton 1953; Prior et al. 1982; Brunsden and Prior 1984). The Persian Gulf has a more or less flat bathymetry with a gentle seaward slope of 0.01% (Sarnthein 1972), but there are subtle small-scale slopes near the northern coastlines (Fig. 8a), especially in the vicinity of Dayyer, which are mainly due to river channels (e.g., Evans 1966) as can be seen in

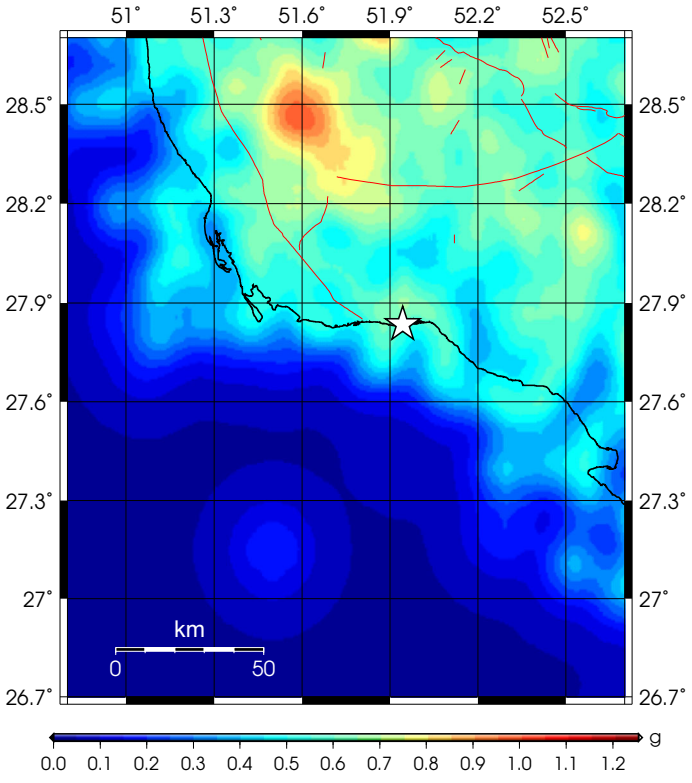

Fig. 10 Peak ground acceleration field calculated for the earthquakes in the IRSC catalog (2006–2017). The white star represents Dayyer. Known fault systems are shown with red lines. Note accelerations reaching 0.6*g* in immediate vicinity of coastline

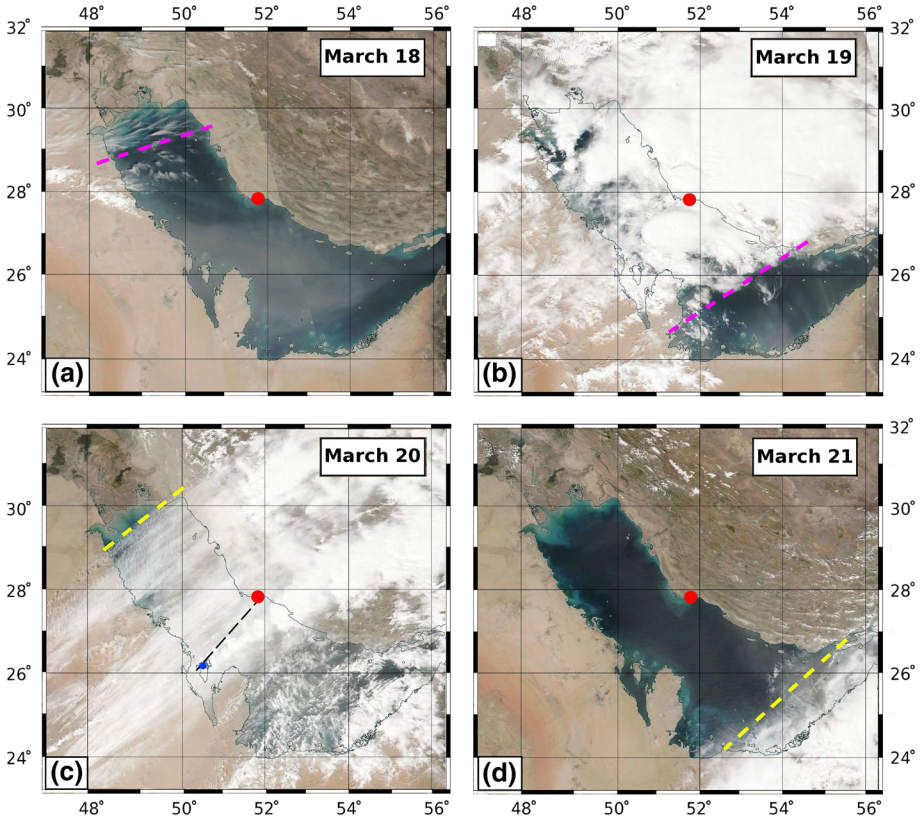

Fig. 11 The shamal system of 18–21 March 2017 from NASA Worldview (2017). The panels **a–d** show satellite images of the Persian Gulf in 24-h snapshots. The pink and yellow dashed lines represent the front and back of the system, respectively. The shamal **a** entered the Gulf on March 18 at a $\sim 70^{\circ}$ azimuth and **b** by the same time the next day, it had travelled ~ 500 km along the Gulf's main axis, suggesting a speed of $\sim$ 6 m/s. **c** After another 24 h, the back of the system entered the Persian Gulf at an azimuth of $\sim 50^{\circ}$, **d** it completely exited the region. The red dot represents the port of Dayyer. The dashed black line connects Dayyer to Bahrain at an azimuth of $\sim 40^{\circ}$

Fig. 8b. Sediments from permanent and seasonal rivers at the northern coastline have built up complex, potentially unstable bathymetry and coastal plains consisting of alluvial, estuarine, deltaic, intertidal mud flat, and beach ridge environments (Evans 1966; Sarnthein 1972). Ross et al. (1986) have also observed a semi-eroded layer adjacent to the Iranian coastlines.

The landslide model can explain some of the observations about the tsunami in question. First, it addresses the more or less calm weather following the storm, especially to the west of Dayyer as suggested by both the field survey and the meteorological reports (e.g., Iran Meteorological Organization, IRIMO 2017). Second, the landslide model may explain why the tsunami was felt only in the close vicinity (a ~ 40 km band of coastline) of Dayyer as suggested by the field survey.

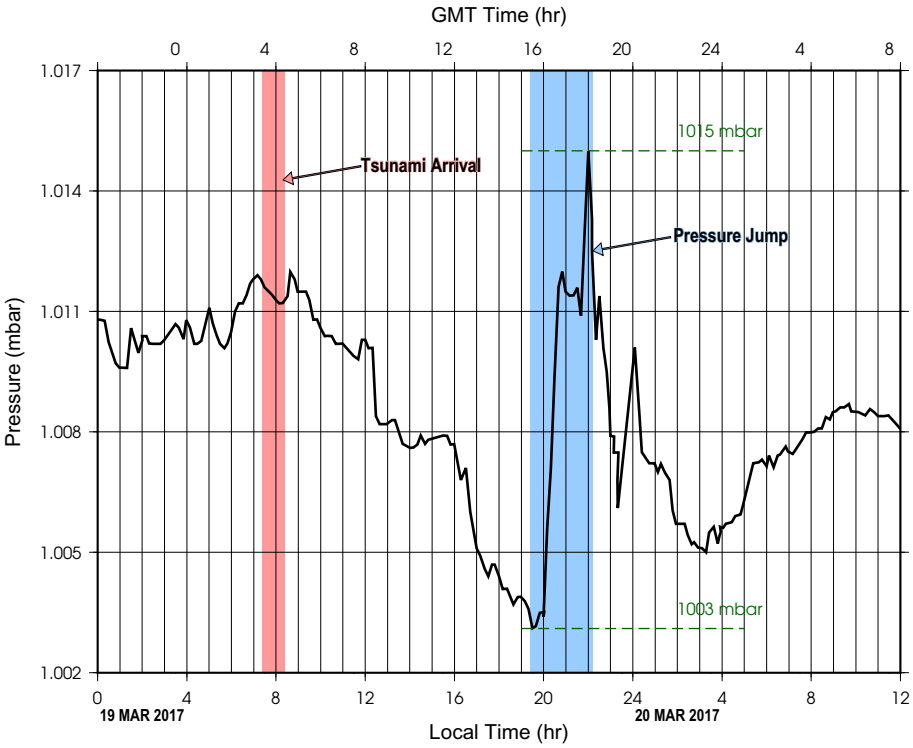

Fig. 12 Atmospheric pressure record sampled at 10-min intervals compiled from 18 meteorological stations across Qatar (personal comm. with Hamad Bin Khalifa University). While the red band marks the occurrence of tsunami in AST (+ 3:00 GMT), the blue band highlights the recorded $\sim$ 12 mbar pressure jump which takes place $\sim$ 13 h later

3.2.1 Landslide triggers

Submarine landslides occur following disturbances in either the pore pressure or viscosity of sediments. Although the triggering process is highly nonlinear and complex, seismic events (e.g., Keefer 1984) and/or storms and rainfall (e.g., Moore 1961) can cause landslides.

3.2.1.1 Seismic trigger The high rate of background seismicity around the northern coastlines of the Persian Gulf (Fig. 9) can cause a high degree of shaking in the region, with seismic hazard assessed locally as moderate to high levels (e.g., Tavakoli and Ghafory-Ashtiany 1999; Giardini et al. 1999). Indeed, Mirzaei et al. (1999) have included Dayyer as well as much of the Bushehr province in a seismic zone with the potential for earthquakes with $6.5 \leq M \leq 7.5$.

We used the algorithm by Campbell and Bozorgnia (2003) to compute the peak ground accelerations for the earthquakes in the IRSC catalog, which includes 2086 events from 2006 to 2017, ranging between $M_L = 1.3$ and 6.3 for this region. Since the majority of these earthquakes have $M_L \leq 4.0$ and therefore no accurate focal geometries, we use a generic unknown focal mechanism for all events, following Campbell and Bozorgnia (2003). We

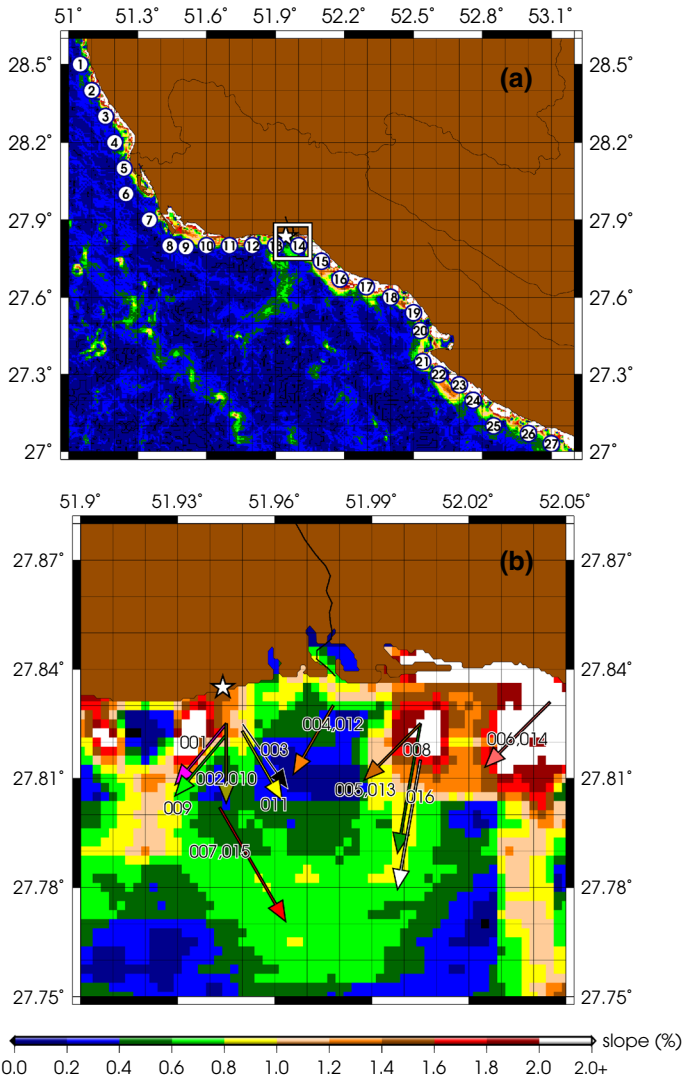

Fig. 13 **a** Slope map of the Persian Gulf in the vicinity of Dayyer; **b** the area inside the white square in **a**. The designed slide dipoles for the larger grid. Size and direction of the arrows represent relative length and azimuth of the dipoles. The white stars in both figures show the location of Dayyer

also applied a moving average window to smooth the results in order to make up for any possible distortions rising from finite sources.

Figure 10 shows the maximum calculated peak acceleration values from all of these earthquakes. As we can see in Fig. 10, accelerations reach $\sim$ 0.6 g on the sea floor, a value well in excess of the triggering threshold as proposed by Keefer (1984). In principle, this level of shaking may have added, during past events, to the slope instability which would eventually have failed on 19 March 2017.

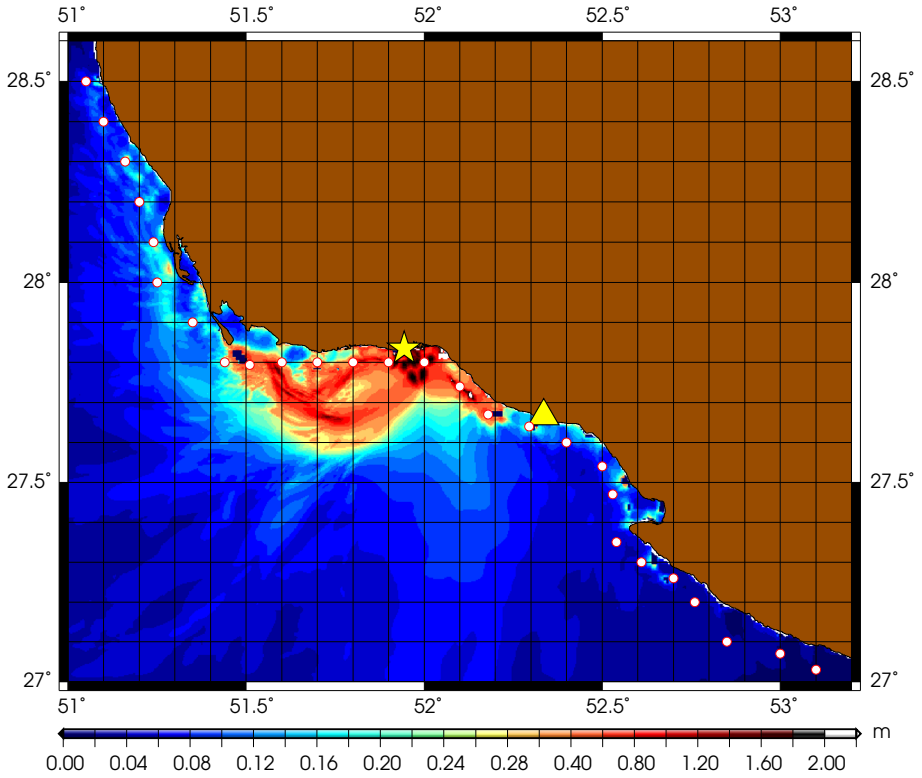

Fig. 14 Maximum amplitudes from landslide dipoles at the coarse grid across all the 16 scenarios. Dayyer and Siraf are shown with yellow star and triangle, respectively. Small dots show the locations of virtual gauges

3.2.1.2 Pressure gradient as trigger In the framework of a landslide-triggered tsunami, the lack of seismicity on and around the event's day suggests that another phenomenon, perhaps the storm on March 19 and the day before (Fig. 11), finally tipped the force balance and resulted in the mass failure causing the tsunami. Although such a statement is only valid in retrospect, we can still apply this model as a tsunami source, due to the highly nonlinear landslide triggering process, the timescale of which may vary from seconds to thousands of years (Weaver and Kuijpers 1983; Masson et al. 2006).

The occurrence of landslides as a result of storm-induced changes in air pressure has been the subject of several studies (e.g., Moore 1961; Larsen and Simon 1993; Baum et al. 1998; Lantuit and Pollard 2008). Although we can analytically study the mechanism of the pressure gradient itself (e.g., Taylor 1948), prediction of the timing of the following mass failure is very difficult and is usually done through statistical methods (e.g., Westen et al. 1997).

Susceptibility of the Persian Gulf region to storms and atmospheric anomalies regularly exposes its coastlines to significant atmospheric pressure perturbations (e.g., Perrone 1979; Reynolds 2002). These atmospheric disturbances occur on both local to regional scales, of which the March 18–21 "shamal" storm detailed below (Sect. 3.3.1.1) is a good example. These systems are usually accompanied by large pressure gradients (e.g., Bitan and

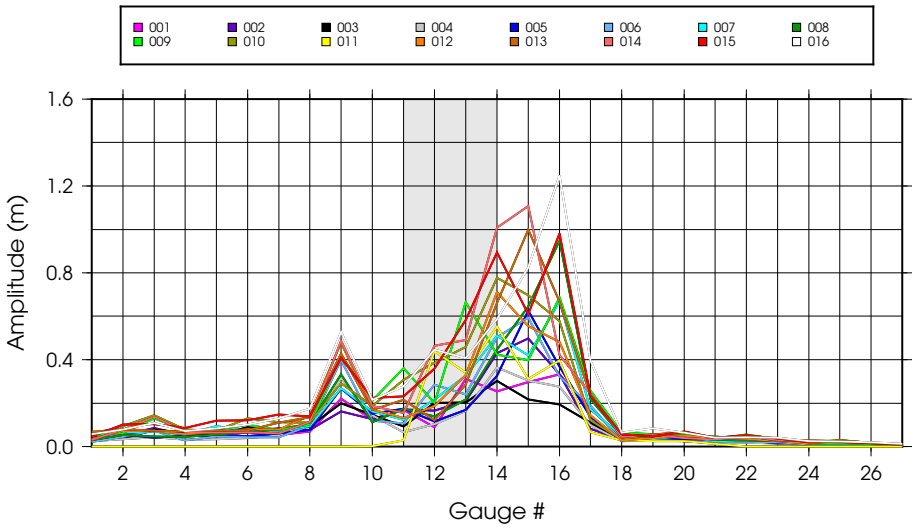

Fig. 15 Maximum computed values of surface elevation at the virtual gauges in Fig. 13a for each of the scenarios shown in Fig. 13b. The curves are color coded to match the arrows in Fig. 13a. The shaded area represents the segment of coastline with maximum observed run-ups

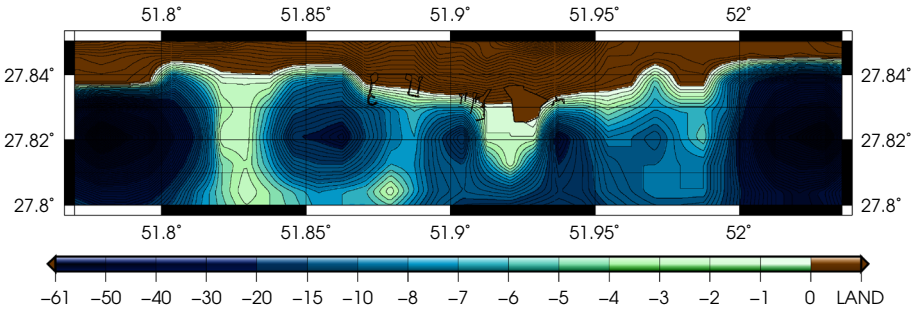

Fig. 16 The interpolated bathymetry grid with resolution of 10 m. The grid boundaries are marked with a large rectangle in Fig. 2

Sa'Aroni (1992)), as readily observed on the March 19 barometric record at Qatar shown on Fig. 12 ($\approx$ 12 mbar), although the signal trails the tsunami by $\sim$ 12 h.

3.2.2 Simulation

Here, we use the block model approach for landslides as proposed by Synolakis et al. (2002) and Okal and Synolakis (2004). In this approach, submarine landslides are modeled as simultaneous hydrodynamic dipoles mirroring the shapes of the initiation and terminal points of the slump. The initial and final points of the slump are reconstructed as, respectively, negative (trough) and positive (hump) hyperbolic trigonometric functions (e.g., Okal et al. 2009; Salaree and Okal 2015).

We simulated the landslide source using the threshold-type MOST—Method Of Splitting Tsunami—algorithm (e.g., Titov and Synolakis 1995, 1998) which has been

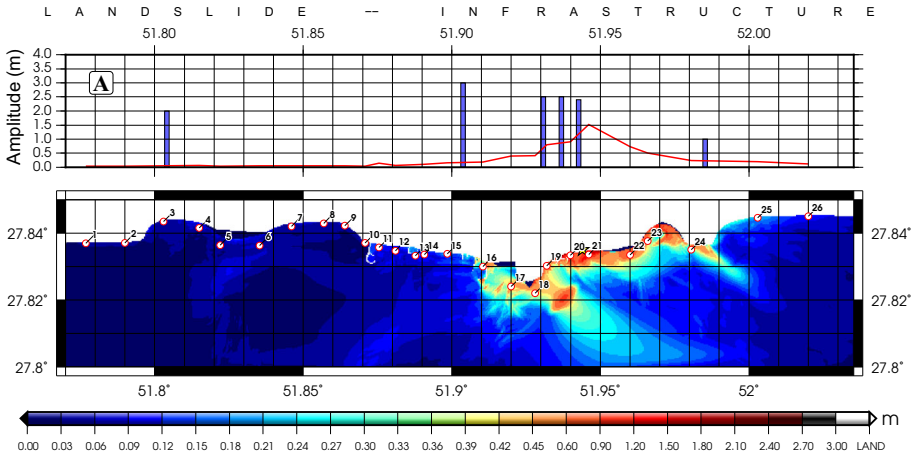

Fig. 17 An example of (bottom) the calculated field of maximum amplitudes in the grid and (top) the maximum amplitudes at the virtual gauges plotted against longitude. The purple bars are measurements from the survey

extensively validated and applied in tsunami field studies (e.g., Titov et al. 2016). In this context, and in the absence of detailed bathymetry maps, we stop the calculation at a depth of 2 m close to the coastline.

3.2.2.1 Natural bathymetry Given the generally small scale of acceptable slides in the Persian Gulf around Dayyer (Fig. 13), we used a grid with a resolution of 9 arc-seconds, interpolated from GEBCO (Fisher et al. 1982), which, to our knowledge, is the best representation of the local bathymetry. This was done to satisfy the sufficiency conditions for the MOST algorithm in terms of the number of grid points in a wavelength, as prescribed e.g., by Shuto et al. (1986) and Titov and Synolakis (1995, 1997). We then designed 16 different slide scenarios according to the slope field of the bathymetry (e.g., Salaree and Okal 2015) as shown in Fig. 13b.

Finally, we used time steps of $\Delta t = 2$ s (considering the very shallow bathymetry of on average ~ 20 m) in order to satisfy the CFL condition (Courant et al. 1928), and performed the simulations for 4-h time windows. Maximum amplitudes at each grid point across all the 16 scenarios are shown in Fig. 14. Time series of surface elevations were computed at 27 virtual gauges shown in Fig. 13a. The maxima of these records for each of the 16 scenarios in Fig. 13b are shown in Fig. 15.

Although our simulations reproduce locally high amplitudes around Dayyer, they either do not predict the highest amplitudes at Oli and Dayyer (gauges 13 and 14), or compute high amplitudes at other places, contradictory to the survey measurements.

3.2.2.2 Considering the infrastructure Because our results with the 9 arc-second resolution do not mirror the observations from the survey, we added small-scale man-made infrastructure to our grid. This may be warranted due to the small dimensions of our dipoles (Titov and Synolakis 1997). Since these structures were built only on a small scale (10–100 m), we built a grid with resolution of ~ 10 m and superimposed them as high altitude blocks with no slopes (Fig. 16). We chose to close the engulfed harbor in Fig. 2 in our simulations due to lack of credible observations from the survey and also to avoid

nonlinear harbor resonance (e.g., Borrero et al. 2015; Synolakis et al. 2016), as such measurements are not necessarily representative of conditions along exposed coasts (e.g., Merrifield et al. 2005). The new grid mainly included the area shown in Fig. 2 since we were considering small-scale dipoles and bathymetry around Dayyer. Finally, we moved the limit of simulation to a depth of 1 m.

We designed six scenarios with different dipole sizes and lengths and conducted the simulations with a time step $\Delta t = 0.3$ s satisfying the CFL condition (Courant et al. 1928). To accommodate the smaller grid size, we use a shorter time window of only 1 h, sufficient to adequately model the interaction with the coastline.

However, as shown in Fig. 17 in the case of one of our scenarios, we still face the issue of run-up concentration. Although the new simulations locate the maximum run-up in Dayyer, they cannot reproduce the distribution of amplitudes around the city, and also

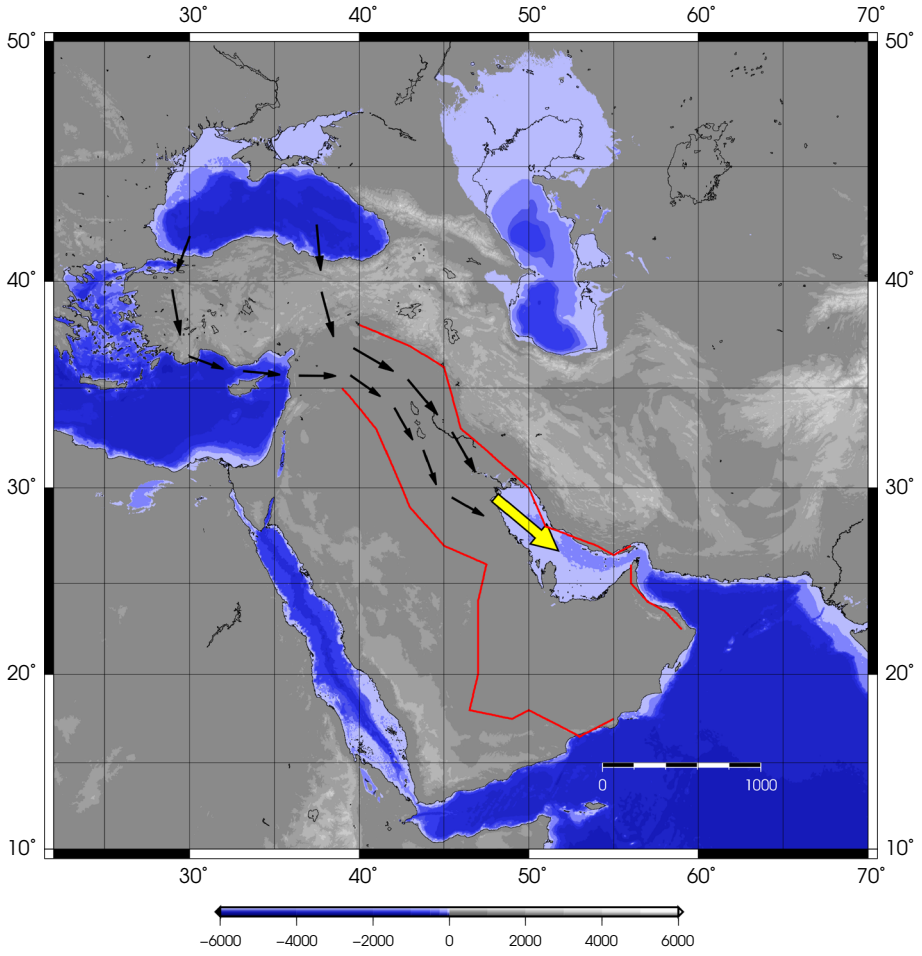

Fig. 18 Topography of the Middle East from the ETOPO1 model (Amante and Eakins 2009). Highlands that create the temperature gradient and channel the wind into the Persian Gulf are marked with red. The black arrows show the paths of cold air into the upper Euphrates valley. The yellow arrow depicts the shamal (modified from Perrone 1979)

completely miss the high amplitudes to the west of Dayyer, especially the 3-m run-up at Oli.

In conclusion, the modeling of the tsunami by an underwater landslide source remains largely unsatisfactory.

3.3 Meteotsunami

The failure of our efforts at modeling the Dayyer tsunami with geological sources, along with the reported atmospheric disturbance, i.e. the storm preceding the event, suggests to treat the surge as a meteotsunami (e.g., Rabinovich and Monserrat 1998; Monserrat and Rabinovich 2006; Pattiaratchi and Wijeratne 2015), the concept of tsunamis being excited by meteorological disturbances going back to Chrystal and Murray (1907). This is made possible in very shallow basins (the Persian Gulf barely approaches 90 m at its deepest point, and averages 34 m) where water gravity waves are slow enough to allow a resonance with the occasional fast-propagating atmospheric disturbance, known as the "Proudman resonance" (Proudman 1929), a model successfully used to explain a number of intriguing tsunamis. Notable among them are the events of 1954 in Lake Michigan, which killed at least 7 people in Chicago (Ewing et al. 1954; Platzman 1958), 1969 in Dwarskersbos, South Africa (Okal et al. 2014), 1992 in Daytona Beach (Churchill et al. 1995; Sallenger et al. 1995), and 2007 in the Georgia Straits, B.C. (Thomson et al. 2009). In several cases, the atmospheric disturbance travelled over large maritime basins, triggering meteotsunamis over hundreds of km and time windows of several days, e.g., in 2014 in the Mediterranean Basin (Šepić et al. 2015), and in 2011 from Portugal to the English Channel (Tappin et al.

Table 2 Maximum wind speeds recorded at the IRIMO stations, sorted with respect to longitude increasing from top to bottom (data from IRIMO 2017; accessed on 3 April 2017)

Lon.	Lat.	Station	Date	Speed (m/s)	Azimuth
48.250	30.367	Abadan	18/3/2014	70	90
49.150	30.550	Bandar Mahshahr	26/10/2008	15	330
49.733	30.283	Hendijan	29/8/2007	23	320
50.167	30.050	Bandar Daylam	20/10/2012	22	210
50.323	29.261	Khark	25/11/2014	13	10
50.817	28.967	Bushehr	26/1/2004	17	290
50.817	28.900	Bushehr (coastal)	29/11/1979	12	150
51.933	27.833	Bandar Dayyer	29/9/1993	13	280
52.367	27.817	Jam Tohid	31/3/1992	12	170
52.735	27.384	Assalooyeh	27/1/2001	12	320
53.383	26.800	Lavan	18/5/2008	20	270
53.983	26.500	Kish	28/2/1983	21	290
54.483	25.883	Siri	24/12/2014	15	280
54.833	26.533	Bandar Lengeh	30/5/2014	30	90
54.833	25.833	Abu Musa	16/3/2014	12	300
55.585	26.955	Bandar Khamir	28/12/2014	26	200
55.917	26.917	Qeshm	27/1/2004	18	210
56.367	27.217	Bandar Abbas	30/7/1986	15	160

2013). In this context, the 2017 Bandar Dayyer tsunami may be most comparable to the Adriatic Sea meteotsunami of 21 June 1978, described in detail by Orlić et al. (2010), and which wrought considerable damage in the Croatian city of Vela Luka.

An important aspect of meteotsunamis is that the atmospheric disturbance creating them need not be of otherwise significant amplitude; in other words, the phenomenon can take place during weather conditions traditionally described as "calm" by the population. Such was the case in 1954 in Chicago, where victims were fishing on a pier; in 1992 in Daytona, where witnesses were celebrating the National Holiday on the beach; in 2007 on Vancouver Island; and in 1969 in Dwarskersbos where a storm of perfectly seasonal characteristics had occurred the night before. In this context, and because they can take place under unsuspected conditions, meteotsunamis constitute an underrated natural hazard (Pattiaratchi and Wijeratne 2015).

3.3.1 Shamal winds

"Shamal winds", the most prominent large-scale meteorological disturbances in the Persian Gulf, are seasonal northwesterly winds that occur during winter and summer (e.g., Perrone 1979; Thoppil and Hogan 2010). The winter shamals occur mainly from November through March and are considered to be relatively rare events with less than 5% exceeding 10 m/s. The summer shamals, however, occur from early June through mid-July and are more frequent but weaker (Perrone 1979). Winter shamals can last anywhere between 24 h to 5 days (Reynolds 2002).

The main reasons for shamal winds are elevation and temperature contrasts in the region (Fig. 18). During the winter months, the high mountains of Turkey, Georgia and Iran channel the cold air from higher latitudes as natural barriers into the low-lying Mesopotamia and Persian Gulf (black arrows in Fig. 18). This results in shallow northwesterly shamals of occasionally extreme strength (up to 70 m/s; IRIMO 2017) creating

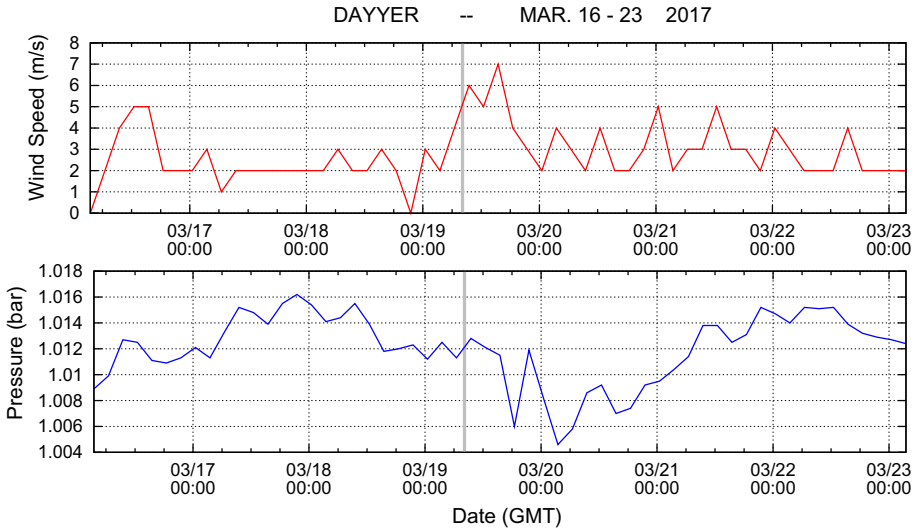

Fig. 19 Wind speed and barometric records from the Dayyer meteorological station sampled at every 3 h (GMT) during 16–23 March 2017 (IRIMO 2017; accessed on 3 April 2017). The thick gray lines represent the arrival time of the tsunami

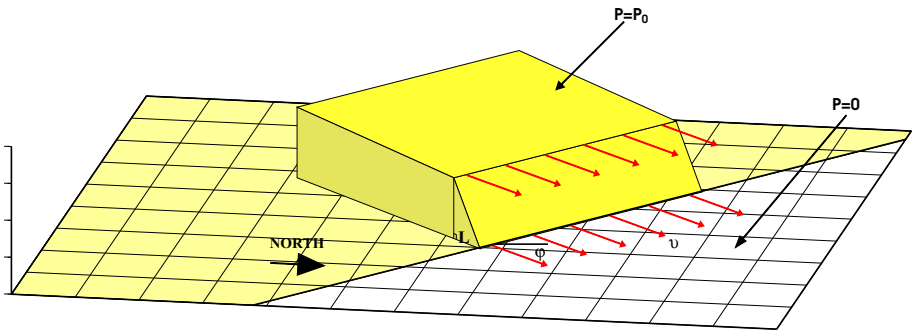

Fig. 20 Schematics of the hypothetical conditions of overpressure. The pressure has non-zero values at the areas shown in yellow, increasing linearly (in the form of a ramp with width L) from $P = 0$ at the front (solid black line) to P_0 at the maximum. The pressure system moves at a uniform velocity v (red arrows) perpendicular to the front with azimuth of ϕ

thunderstorms and advecting dust and sand over the Persian Gulf region (Table 2), which continue until the low pressure trough slowly exits the Strait of Hormuz and is replaced by local sea breezes (Perrone 1979).

On average, shamal winds have celerities between 7 and 10 m/s, insufficient to elicit resonance with gravity waves in most of the Gulf, but values of 15–20 m/s are common along the southern coastlines. The area of Lavan Island (southeast of Dayyer) and the northern vicinity of Qatar can feature winds 5–7 m/s faster than average (Perrone 1979). Maximum recorded speeds at the Iranian meteorological stations on the Persian Gulf are given in Table 2. The pressure gradient between Saudi Arabia and Iraq can range from 5 to 15 mbar. If the shamal lasts for more than 2 days, speeds of 17–22 m/s may result in the southern Gulf where the pressure gradient is strongest (Perrone 1979).

As a result of the shamals, short period ($\sim$ 12 h) sea level rises of $\sim$ 3–4 m occur. However, such sea rises take the form of long lasting surges rather than short-lived waves. In areas with stronger winds such as the southern coastlines, the sea level rises happen more quickly and are $\sim$ 1 m higher (Perrone 1979). Following the end of 3–5 day shamals, swells may persist for up to three days.

3.3.1.1 The 19 March 2017 storm system We were able to investigate the weather conditions around the time of the Dayyer tsunami based on meteorological data, which however remain fragmentary. NASA Worldview daily satellite imagery (Fig. 11) suggests a strong northwesterly shamal system moving across the Gulf at an average speed of $\sim$ 7–8 m/s over an interval of three days. In addition, we obtained pressure and wind speed data at Qatar (Fig. 12) and at IKUWAIT22 (Kuwait) and IJASRA2 (Bahrain) stations, showing jumps in pressure of 6 to 12 mbar on March 19, around 20:00, 15:15 and 19:15 (GMT+3), respectively. Wind speed and pressure records were also obtained at Dayyer proper (Fig. 19), but they show no significant signals on the 19th, in agreement with the generally smaller expression of the shamal systems on the Iranian side of the Gulf. Note, however, the extremely coarse sampling of the Dayyer data (one point every 3 h) which does not lend them to meaningful data processing.

The records from the Bahraini and Qatari stations are particularly important. Given the orientation of the shamal system on the 19th, the weather front should have arrived at

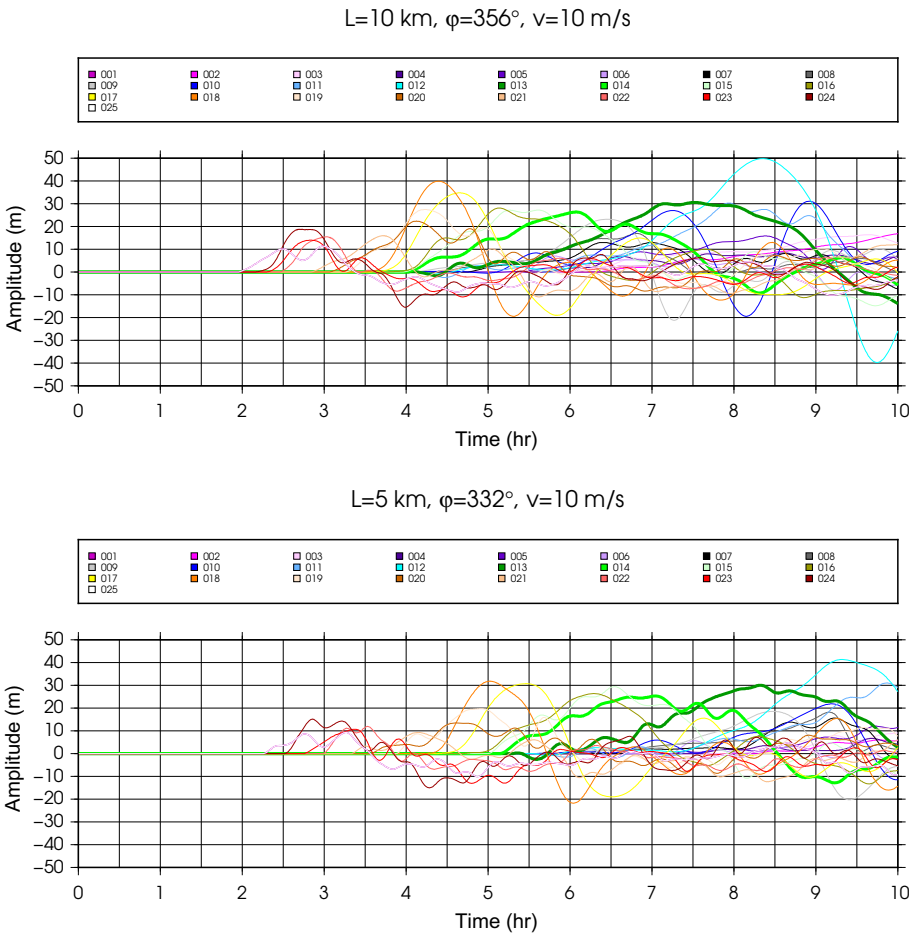

Fig. 21 Time series at the 25 gauges for the two scenarios with maximum calculated amplitudes in the vicinity of Dayyer. The top and bottom scenarios correspond to Fig. 22a, b, respectively. Gauges 13 and 14 are depicted with thick curves

Dayyer about 2 h earlier than in Bahrain, and 3 h earlier than in Qatar, and thus about 10 h after the tsunami, violating causality for the latter's generation.

This would suggest that any possible atmospheric disturbance responsible for the tsunami must have been of an ancillary nature to the main shamal; consequently, we will perform our simulations of the event on a local scale.

3.3.2 Simulation

Following the approach by Platzman (1958), we consider a squall with the cross-section of a ramp, moving at a given velocity perpendicular to the front (Fig. 20). We then solve the shallow-water version of the Navier–Stokes equation for an incompressible flow as

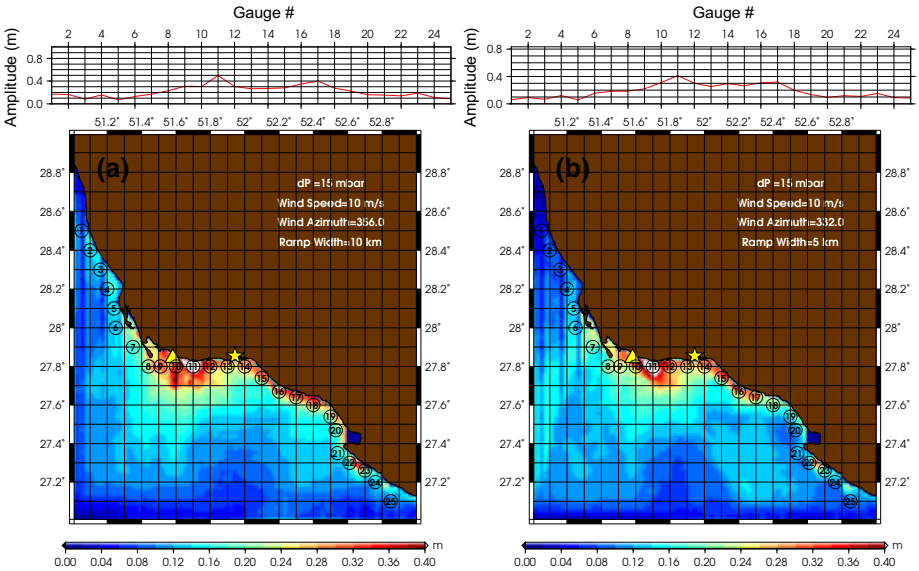

Fig. 22 Maximum calculated amplitudes at (bottom) each grid point and (top) the virtual gauges when **a** gauge 13 (west of Dayyer) and **b** gauge 14 (east of Dayyer) reach their respective maximum wave amplitudes across all simulations

$$\frac{\partial \vec{M}}{\partial t} = D\left(\vec{F} - g\vec{\nabla}h\right) \tag{1}$$

where g is the acceleration of gravity. In Eq. (1), D and h are the depth of water column and the vertical displacement at any given point, while $\vec{M}$ is the volume transport vector (velocity integraled over depth),

$$\vec{M} = \int_{-D}^{h} \vec{U}\,\mathrm{d}z \tag{2}$$

and $\vec{F} = -\frac{\vec{\nabla}P}{\rho}$ is the atmospheric pressure gradient force. In writing Eqs. (1) and (2), we have used the conditions for the "Proudman resonance" where the gravity waves move at the speed of the pressure gradient (e.g., Proudman 1929; Orlić 1980; Šepić et al. 2009; Okal et al. 2014). We consider only linear terms and assume the pressure to be purely hydrostatic. We also neglect the Coriolis force and lateral frictions (Dean and Dalrymple 1991).

A finite difference algorithm was used to solve Eqs. (1) and (2). We used an interpolated version of GEBCO bathymetry data (Fisher et al. 1982) for the water depth and time steps of $\delta t = 30$ s to satisfy the CFL condition in 10 h time windows. The pressure step of the front was taken as 15 mbar. By varying its ramp length, L, from 0 to 100 km at 5 km increments, wind celerity, v, from 10 to 30 m/s with 1 m/s increments, and propagation azimuth, ϕ, between 0° and 359° with 1° steps, we conducted a total of 158,760 simulations to find the ideal conditions for maximum amplitude in the vicinity of Dayyer.

Time series of water level values were also recorded at 25 virtual gauges along the coastline, as presented in Fig. 21a, b. These figures suggest that a larger wave, mixed with

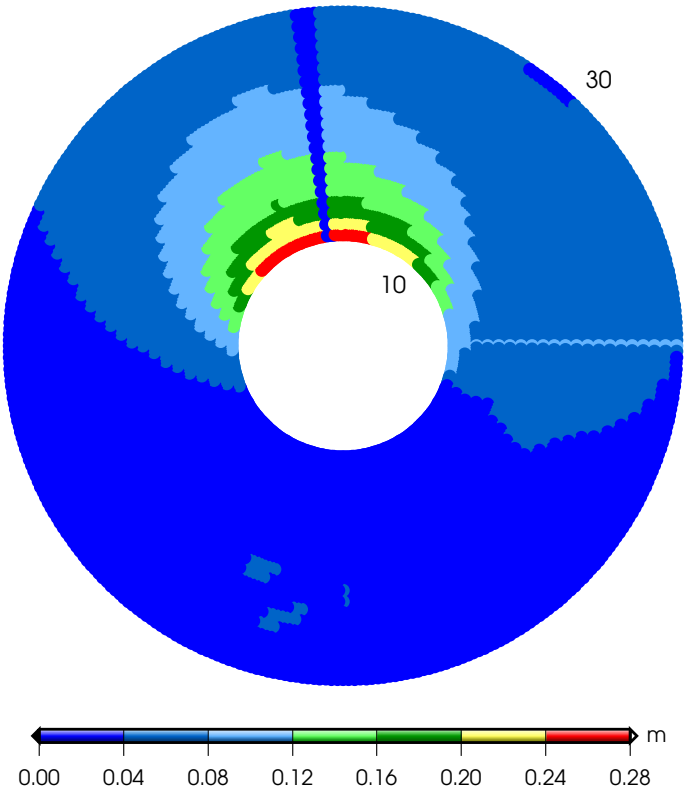

Fig. 23 Maximum calculated amplitudes at Dayyer as a function of propagation azimuth (0°–359°), and wind celerity (10–30 m/s) at a ramp length of 10 km

a few (perhaps two) smaller signals, would arrive at Dayyer in a maximum amplitude scenario.

Our simulations predict the maximum amplitudes at gauges 13 and 14—at both sides of Dayyer—to occur for ($L = 10$ km, $\phi = 356°$, $v = 10$ m/s) or ($L = 5$ km, $\phi = 332°$, $v = 10$ m/s), respectively (Fig. 22a, b). More generally and as shown in Fig. 23, almost no high amplitudes are created at Dayyer for an azimuth of $\sim 130°$, i.e. the direction of the shamal, but rather amplitudes are concentrated at Dayyer for wind systems propagating in a generally northward direction.

Although the simulations predict $\sim$ 30–40 cm of amplitude in the vicinity of Dayyer, the maximum calculated amplitudes are concentrated at the promontory to the west of Dayyer as can be seen in Fig. 24 which shows maximum amplitudes at each grid point across all the simulations. This could be due to the abrupt changes in bathymetry near Motaf (points 1–4 in Table 1) which causes the waves to increase in size. However, the absolute maximum at Oli is not reproduced.

There remains the issue of causality, the Dayyer tsunami preceding the main barometric signals from the Shamal winds at the relevant longitudes by $\sim$11 h. While this negates a direct Proudman resonance with them, the model we propose here is that of a Proudman resonance with a smaller and precursory system, propagating Northwards, and which would have been ancillary to the main Shamal system.

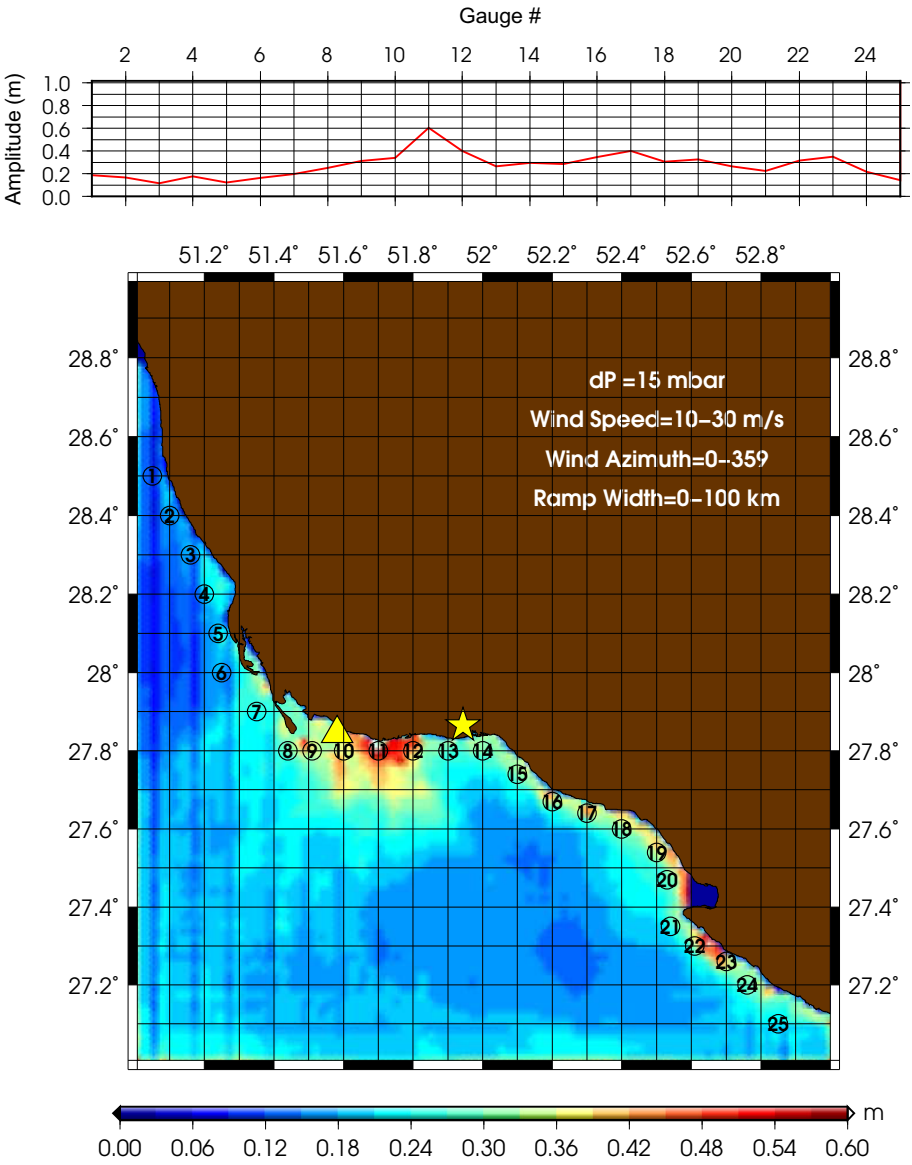

Fig. 24 Maximum calculated amplitudes at (bottom) each grid point and (top) 25 virtual gauges (from west to east) across all the 158,760 simulations. Dayyer and Motaf are depicted by a star and a triangle, respectively. The circles show the virtual gauges where water level fluctuations are recorded

In summary, our meteorological simulations provide a generally more acceptable fit to our surveyed dataset.

4 Discussion and conclusion

Following the singular event at Bandar Dayyer on 19 March 2017, our field survey has resulted in a database, summarized in Table 1 and Fig. 3, whose principal features are an inundated segment of coastline extending $\sim$ 40 km around the city of Dayyer, with the highest values concentrated over a much narrower ($\sim$ 8 km) stretch of the coast, from the village of Oli in the West to the city of Dayyer in the East. This distribution constitutes the main feature to be fit by any modeling attempt; it suggests a small and local structure as the origin of the tsunami.

A seismic source for the Dayyer tsunami can easily be ruled out based on the absence of sufficiently large earthquakes on that day (Fig. 7), leaving either landslides or meteorological disturbances as viable sources for the event.

The possibility of an underwater landslide as the source of the tsunami is controlled by the presence of a sufficient slope in the field of the gradient of bathymetry. However, based upon presently available models of bathymetry, the locations of the only legitimate such sources predict a distribution of tsunami amplitude significantly displaced eastwards (by about 20 km) with respect to Dayyer (Figs. 14, 15). This could be due to the use of inaccurate small-scale bathymetry, obtained by interpolating the GEBCO grid to satisfy the small-scale requirements of our calculation; this interpolation process, although mathematically accurate, may not reproduce actual, subtle, variations in depth, and because it is in the nature of a smoothing agent, could particularly affect the gradient of bathymetry in the form of the size, length and azimuths of the potential slides, which in turn directly affect our simulations (e.g., Salaree and Okal 2015). We note, however, that our attempt to model the influence of recently built port infrastructure has failed to significantly improve the fit of our simulated run-up profiles to the results of our survey.

An underwater landslide could conceivably have been detected by hydroacoustic stations inside the Gulf, or by seismic stations deployed in the immediate vicinity of shorelines in the geometry of the so-called "*T*-phase stations" (Okal 2001, 2003). Unfortunately, both the stations of the Iranian national network (LMD1 and QIR1) and the lone IRIS-GSN station in the region (UOSS, UAE) are located more than 100 km from the shorelines; we know of no accessible regional records from either hydrophone or island stations. In addition, we note that the water column in the Gulf does constitute a low velocity waveguide, but its very shallow character (at most 70 m or roughly ten times less than the typical SOFAR channel in the world's oceans) will only trap waves of very high frequency (20 Hz or higher), which are poorly generated by landslide sources systematically red-shifted with respect to their seismic counterparts (Okal 2003), and would not propagate onland after conversion at a receiver shoreline. Thus, the prospects of independently identifying an underwater landslide as the source of this tsunami appear bleak.

In general terms, we prefer the atmospheric model, since it provides a generally better fit to the distribution of tsunami amplitudes obtained in our survey (generally west of Dayyer) than predicted by the landslide models (generally east of Dayyer); the predictions for Motaf Park remain, however, too large.

It is also noteworthy that meteotsunami simulations at gauge 14 (west Dayyer) predict a dominant wave superimposed by two smaller signals (Fig. 21a) as described to us during the survey. At gauge 13 (eastern coast of Dayyer), however, we only see one wave in our simulations as shown in Fig. 21.

In addition, the atmospheric models suffer from the fact that the concentration of the wave along an approximately East–West coastline at Dayyer requires coupling with a

weather system moving in the 332° or 356° azimuths, i.e., essentially North–South, while the major weather system observed at the time, the shamal, was propagating along ~N135°E. This requires that the parent weather system for the tsunami be a secondary or ancillary effect of the shamal which, while legitimate, remains undocumented.

Finally, we address the possibility of the Dayyer tsunami being an instance of a "sneaker wave". Such phenomena, of which a number were described, e.g., by Didenkulova et al. (2006), are generally considered to be the result of nearshore shoaling of deep-water "rogue waves" (Soomere 2010). We regard this interpretation as unlikely, given that the Dayyer tsunami featured a series of at least three waves, whereas rogue waves usually consist of a single one (Kharif and Pelinovsky 2003) and are generated in much deeper water than the Persian Gulf, and that to our knowledge, no rogue wave with the potential of fostering a sneaker wave on the Iranian coast was documented on 19 March 2017 inside the Persian Gulf, an area well known for its heavily travelled shipping lanes.

In summary, neither geological nor atmospheric sources can perfectly explain the distribution of amplitudes as obtained in our field survey. While we prefer the meteorological model, we suggest that its remaining misfits may be due to imprecisions in small-scale bathymetry and that future studies of the 19 March 2017 tsunami would warrant the use of a better bathymetry model for the region.

Acknowledgements The authors wish to thank Persian Gulf University for their help on the field survey. We thank Mohammed Ayoub and Marwan Khraisheh of Qatar Environment and Energy Research Institute (QEERI) at Hamad Bin Khalifa University who provided us with the Qatari barometric records. The original version of the paper was improved by the comments of A. B. Rabinovich and two anonymous reviewers. We are also grateful to Douglas MacAyeal for pointing us to the NASA dataset of atmospheric imagery. Some of the figures were created using the Generic Mapping Tools (Wessel and Smith 1991) and Gnuplot (Williams and Kelley 2009) packages.

References

Abe K (2005) Tsunami resonance curve from dominant periods observed in bays of northeastern Japan. In: Satake K (ed) Tsunamis: Case studies and recent developments. Springer, pp 97–113

Abe Ku, Abe Ka, Tsuji Y, Imamura F, Katao H, Iio Y, Satake K, Bourgeois J, Noguera E, Estrada F (1993) Field survey of the Nicaragua earthquake and tsunami of September 2, 1992. Bull Earthq Res Inst Tokyo Univ 68:23–70

Amante C, Eakins BW (2009) ETOPO1 1 arc-minute global relief model: procedures, data sources and analysis. US Department of Commerce, National Oceanic and Atmospheric Administration, National Environmental Satellite, Data, and Information Service, National Geophysical Data Center, Marine Geology and Geophysics Division, Boulder, Colorado

Ambraseys NN (2008) Descriptive catalogues of historical earthquakes in the Eastern Mediterranean and the Middle East; Revisited. In: Fréchet J, Meghraoui M, Stucchi M (eds) Historical seismology. Modern approaches in solid earth sciences, vol 2. Springer, Dordrechtpp, pp 25−39

Ambraseys NN, Melville CP (1982) A history of Persian earthquakes. Cambridge University Press, Cambridge

Baum RL, Chleborad AF, Schuster RL (1998) Landslides triggered by the winter 1996–97 storms in the Puget Lowland, Washington. Technical report, US Department of the Interior, US Geological Survey:[Branch of Information Services, distributor]

Bitan A, Sa'Aroni H (1992) The horizontal and vertical extension of the Persian Gulf pressure trough. Int J Climatol 12(7):733–747

Borrero JC, Lynett PJ, Kalligeris N (2015) Tsunami currents in ports. Philos Trans R Soc A 373(2053):20140372

Brunsden D, Prior DB (1984) Slope instability. Wiley, New York

Campbell KW, Bozorgnia Y (2003) Updated near-source ground-motion (attenuation) relations for the horizontal and vertical components of peak ground acceleration and acceleration response spectra. Bull Seismol Soc Am 93(1):314–331
Chrystal G, Murray J (1907) An investigation of the seiches of Loch Earn by the Scottish Lake survey. Trans R Soc Edinb 45(02):361–396
Churchill DD, Houston SH, Bond NA (1995) The Daytona Beach wave of 3–4 July 1992: a shallow-water gravity wave forced by a propagating squall line. Bull Am Meteorol Soc 76(1):21–32
Courant R, Friedrichs K, Lewy H (1928) Über die partiellen Differenzengleichungen der mathematischen Physik. Math Ann 100(1):32–74
Dean RG, Dalrymple RA (1991) Water wave mechanics for engineers and scientists, vol 2. World scientific publishing Co Inc, Singapore
Didenkulova I, Slunyaev A, Pelinovsky E, Kharif C (2006) Freak waves in 2005. Nat Hazards Earth Syst Sci 6(6):1007–1015
Dziewonski A, Chou T-A, Woodhouse J (1981) Determination of earthquake source parameters from waveform data for studies of global and regional seismicity. J Geophys Res Solid Earth 86(B4):2825–2852
Ekström G, Nettles M, Dziewoński A (2012) The global CMT project 2004–2010: centroid-moment tensors for 13,017 earthquakes. Phys Earth Planet Inter 200:1–9
Evans G (1966) The recent sedimentary facies of the Persian Gulf region. Philos Trans R Soc Lond A Math Phys Eng Sci 259(1099):291–298
Ewing M, Press F, Donn W L (1954) An explanation of the Lake Michigan wave of 26 June 1954. Science 120:684–686
Fisher R, Jantsch M, Comer R (1982) General bathymetric chart of the oceans (GEBCO). Canadian hydrographic Service, Ottawa
Fritz HM, Phillips DA, Okayasu A, Shimozono T, Liu H, Mohammed F, Skanavis V, Synolakis CE, Takahashi T (2012) The 2011 Japan tsunami current velocity measurements from survivor videos at Kesennuma Bay using LiDAR. Geophys Res Lett 39(7):L00G23. https://doi.org/10.1029/2011GL050686
Geller RJ (1976) Scaling relations for earthquake source parameters and magnitudes. Bull Seismol Soc Am 66(5):1501–1523
Giardini D, Grünthal G, Shedlock KM, Zhang P (1999) The GSHAP global seismic hazard map. Ann Geophys 42(6):1225–1230
IRIMO (2017) I.R. of Iran Meteorological Organization. http://www.irimo.ir. Accessed 3 Apr 2017
Keefer DK (1984) Landslides caused by earthquakes. Geol Soc Am Bull 95(4):406–421
Kharif C, Pelinovsky E (2003) Physical mechanisms of the rogue wave phenomenon. Eur J Mech B/Fluids 22(6):603–634
Lamb A (1964) A visit to Siraf, an ancient port on the Persian Gulf. J Malays Branch R Asiat Soc 37(1(205)):1–19
Lantuit H, Pollard W (2008) Fifty years of coastal erosion and retrogressive thaw slump activity on Herschel Island, southern Beaufort Sea, Yukon Territory, Canada. Geomorphology 95(1):84–102
Larsen MC, Simon A (1993) A rainfall intensity-duration threshold for landslides in a humid-tropical environment, Puerto Rico. Geografiska Annaler Ser A Phys Geogr 75:13–23
Ma G, Kirby JT, Shi F (2013) Numerical simulation of tsunami waves generated by deformable submarine landslides. Ocean Model 69:146–165
Masson D, Harbitz C, Wynn R, Pedersen G, Løvholt F (2006) Submarine landslides: processes, triggers and hazard prediction. Philos Trans R Soc Lond A Math Phys Eng Sci 364(1845):2009–2039
Merrifield M, Firing Y, Aarup T, Agricole W, Brundrit G, Chang-Seng D, Farre R, Kilonsky B, Knight W, Kong L et al (2005) Tide gauge observations of the Indian Ocean tsunami, December 26, 2004. Geophys Res Lett 32(9):L09603 4 pp
Miller GS, Andy Take W, Mulligan RP, McDougall S (2017) Tsunamis generated by long and thin granular landslides in a large flume. J Geophys Res Oceans 122(1):653–668
Mirzaei N, Gao M, Chen Y-T (1999) Delineation of potential seismic sources for seismic zoning of Iran. J Seismol 3(1):17–30
Mirzaei N, Gheitanchi M, Naserieh S, Raeesi M, Zarifi Z, Tabaei S-G (2002) Basic parameters of earthquakes in Iran. DaneshNegar Publ, Tehran
Monserrat S, Rabinovich A et al (2006) Meteotsunamis: atmospherically induced destructive ocean waves in the tsunami frequency band. Nat Hazards Earth Syst Sci 6(6):1035–1051
Moore DG (1961) Submarine slumps. J Sediment Res 31(3):343–357
NASA Worldview (2017) Earth observing system data and information system. NASA's Earth Science Data Systems. https://worldview.earthdata.nasa.gov. Accessed 20 May 2017

Okal EA (2001) T-phase stations for the international monitoring system of the comprehensive nuclear-test ban treaty: a global perspective. Seismol Res Lett 72(2):186–196
Okal EA (2003) T waves from the 1998 Papua New Guinea earthquake and its aftershocks: timing the tsunamigenic slump. Pure Appl Geophys 160(10–11):1843–1863
Okal EA, Synolakis CE (2003) A theoretical comparison of tsunamis from dislocations and landslides. Pure Appl Geophys 160(10–11):2177–2188
Okal EA, Synolakis CE (2004) Source discriminants for near-field tsunamis. Geophys J Int 158(3):899–912
Okal EA, Synolakis CE, Fryer GJ, Heinrich P, Borrero JC, Ruscher C, Arcas D, Guille G, Rousseau D (2002) A field survey of the 1946 Aleutian tsunami in the far field. Seismol Res Lett 73(4):490–503
Okal EA, Fritz H, Sladen A (2009a) 2004 Sumatra-Andaman tsunami surveys in the Comoro islands and Tanzania and regional tsunami hazard from future Sumatra events. S Afr J Geol 112(3–4):343–358
Okal EA, Synolakis CE, Uslu B, Kalligeris N, Voukouvalas E (2009b) The 1956 earthquake and tsunami in Amorgos, Greece. Geophys J Int 178(3):1533–1554
Okal EA, Visser JN, de Beer CH (2014) The Dwarskersbos, South Africa local tsunami of August 27, 1969: field survey and simulation as a meteorological event. Nat Hazards 74(1):251–268
Orlić M (1980) About a possible occurrence of the Proudman resonance in the Adriatic. Thalassia Jugoslavica 16(1):79–88
Orlić M, Belušić D, Janeković I, Pasarić M (2010) Fresh evidence relating the great Adriatic surge of 21 June 1978 to mesoscale atmospheric forcing. J Geophys Res Oceans 115(C6):C06011. https://doi.org/10.1029/2009JC005777
Pattiaratchi CB, Wijeratne E (2015) Are meteotsunamis an underrated hazard? Philos Trans R Soc A 373(2053):20140377
Perrone TJ (1979) Winter shamal in the Persian Gulf. Technical report, Naval Environmental Prediction Research Facility Monterey, CA
Plafker G (1997) Catastrophic tsunami generated by submarine slides and backarc thrusting during the 1992 earthquake on eastern Flores I., Indonesia. In: Geological Society of America, Cordilleran Section, 93rd Annual Meeting, vol 29, no 5, p 57
Platzman GW (1958) A numerical computation of the surge of 26 June 1954 on Lake Michigan. University of Chicago, Department of Meteorology
Prior DB, Bornhold BD, Coleman JM, Bryant WR (1982) Morphology of a submarine slide, Kitimat Arm, British Columbia. Geology 10(11):588–592
Proudman J (1929) The effects on the sea of changes in atmospheric pressure. Mon Not R Astron Soc Geophys Suppl 2(s4):197–209
Rabinovich AB (1997) Spectral analysis of tsunami waves: separation of source and topography effects. J Geophys Res Oceans 102(C6):12663–12676
Rabinovich AB, Monserrat S (1998) Generation of meteorological tsunamis (large amplitude seiches) near the Balearic and Kuril Islands. Nat Hazards 18(1):27–55
Reynolds R (2002) Meteorology and climate. In: The Gulf ecosystem: health and sustainability. Backhuys, Leiden, pp 53–64
Rodis S (2017) What's the tide? http://www.whatsthetide.com. Accessed 2 Aug 2017
Ross DA, Uchupi E, White RS (1986) The geology of the Persian Gulf–Gulf of Oman region: a synthesis. Rev Geophys 24(3):537–556
Salaree A, Okal EA (2015) Field survey and modelling of the Caspian Sea tsunami of 1990 June 20. Geophys J Int 201(2):621–639
Sallenger AH, List JH, Gelfenbaum G, Stumpf RP, Hansen M (1995) Large wave at Daytona Beach, Florida, explained as a squall-line surge. J Coast Res 11:1383–1388
Sarnthein M (1972) Sediments and history of the postglacial transgression in the Persian Gulf and northwest Gulf of Oman. Mar Geol 12(4):245–266
Šepić J, Vilibić I, Belušić D (2009) Source of the 2007 Ist meteotsunami (Adriatic Sea). J Geophys Res Oceans 114(C3):C03016. https://doi.org/10.1029/2008JC005092
Šepić J, Vilibić I, Rabinovich AB, Monserrat S (2015) Widespread tsunami-like waves of 23–27 June in the Mediterranean and Black Seas generated by high-altitude atmospheric forcing. Sci Rep 5:11682
Shuto N, Suzuki T, Hasegawa K (1986) A study of numerical techniques on the tsunami propagation and run-up. Sci Tsunami Hazard 4:111–124
Skempton A (1953) Soil mechanics in relation to geology. Proc Yorks Geol Soc 29(1):33–62
Soomere T (2010) Rogue waves in shallow water. Eur Phys J Spec Top 185(1):81–96
Synolakis C, Imamura F, Tsuji Y, Matsutomi H, Tinti S, Cook B, Chandra Y, Usman M (1995) Damage, conditions of East Java tsunami of 1994 analyzed. EOS Trans Am Geophys Union 76(26):257–257

Synolakis CE, Bardet J-P, Borrero JC, Davies HL, Okal EA, Silver EA, Sweet S, Tappin DR (2002) The slump origin of the 1998 Papua New Guinea tsunami. Proc Roy Soc (London) Ser A 458(2020):763–789

Synolakis C, Maravelakis N, Kalligeris N, Skanavis V, Kânoğlu U, Yalçıner A, Lynett P (2016) Case study of small harbor excitation under storm and tsunami conditions. In: EGU general assembly conference abstracts, vol 18. Paper no 13825

Tappin DR, Sibley A, Horsburgh K, Daubord C, Cox D, Long D (2013) The English Channel tsunami of 27 June 2011-a probable meteorological source. Weather 68(6):144–152

Tavakoli B, Ghafory-Ashtiany M (1999) Seismic hazard assessment of Iran. Ann Geophys 42(6):1013–1021

Taylor DW (1948) Fundamentals of soil mechanics, vol 66. LWW, Philadelphia

ten Brink US, Lee HJ, Geist EL, Twichell D (2009) Assessment of tsunami hazard to the US East Coast using relationships between submarine landslides and earthquakes. Mar Geol 264(1):65–73

Thomson R, Rabinovich A, Fine I, Sinnott D, McCarthy A, Sutherland N, Neil L (2009) Meteorological tsunamis on the coasts of British Columbia and Washington. Phys Chem Earth Parts A/B/C 34(17):971–988

Thoppil PG, Hogan PJ (2010) Persian Gulf response to a wintertime shamal wind event. Deep Sea Res Part I Oceanogr Res Pap 57(8):946–955

Titov VV, Synolakis CE (1995) Modeling of breaking and nonbreaking long-wave evolution and runup using VTCS-2. J Waterw Port Coast Ocean Eng 121(6):308–316

Titov VV, Synolakis CE (1997) Extreme inundation flows during the Hokkaido-Nansei-Oki tsunami. Geophys Res Lett 24(11):1315–1318

Titov VV, Synolakis CE (1998) Numerical modeling of tidal wave run-up. J Waterw Port Coast Ocean Eng 124(4):157–171

Titov V, Kânoğlu U, Synolakis C (2016) Development of MOST for real-time tsunami forecasting. J Waterw Port Coast Ocean Eng 142:03116004-1–03116004-16

Tofighian H (2014) Architectural analysis of the coastal segment of the Port of Siraf through underwater archaeological studies. Archaeol Stud 6(1):21–38

Van Westen CJ, Rengers N, Terlien M, Soeters R (1997) Prediction of the occurrence of slope instability phenomena through GIS-based hazard zonation. Geol Rundsch 86(2):404–414

Weaver P, Kuijpers A (1983) Climatic control of turbidite deposition on the Madeira Abyssal Plain. Nature 306(5941):360–363

Weiss R, Krastel S, Anasetti A, Wünnemann K (2013) Constraining the characteristics of tsunami waves from deformable submarine slides. Geophys J Int 194:316–321

Wessel P, Smith WH (1991) Free software helps map and display data. EOS Trans Am Geophys Union 72(41):441 and 445–446

Whitehouse D (1968) Excavations at Sīrāf; first interim report. Iran 6:1–22

Williams T, Kelley C (2009) Gnuplot 4.2: an interactive plotting program. http://gnuplot.sourceforge.net/